

The chemical composition of Galactic ring nebulae around massive stars

C. Esteban,^{1,2*} A. Mesa-Delgado,³ C. Morisset⁴ and J. García-Rojas^{1,2}

¹*Instituto de Astrofísica de Canarias, E-38200 La Laguna, Tenerife, Spain*

²*Departamento de Astrofísica, Universidad de La Laguna, E-38206, La Laguna, Tenerife, Spain*

³*Instituto de Astrofísica, Facultad de Física, Pontificia Universidad Católica de Chile, Av. Vicuña Mackenna 4860, 782-0436 Macul, Santiago, Chile*

⁴*Instituto de Astronomía, Universidad Nacional Autónoma de México, Apdo. Postal 70264, 04510 México D.F., Mexico*

Accepted XXX. Received YYY; in original form ZZZ

ABSTRACT

We present deep spectra of ring nebulae associated with Wolf-Rayet (WR) and O-type stars: NGC 6888, G2.4+1.4, RCW 58, S 308, NGC 7635 and RCW 52. The data have been taken with the 10m Gran Telescopio Canarias and the 6.5m Clay Telescope. We extract spectra of several apertures in some of the objects. We derive C²⁺ and O²⁺ abundances from faint recombination lines in NGC 6888 and NGC 7635, permitting to derive their C/H and C/O ratios and estimate the abundance discrepancy factor (ADF) of O²⁺. The ADFs are larger than the typical ones of normal H II regions but similar to those found in the ionised gas of star-forming dwarf galaxies. We find that chemical abundances are rather homogeneous in the nebulae where we have spectra of several apertures: NGC 6888, NGC 7635 and G2.4+1.4. We obtain very high values of electron temperature in a peripheral zone of NGC 6888, finding that shock excitation can reproduce its spectral properties. We find that all the objects associated with WR stars show N enrichment. Some of them also show He enrichment and O deficiency as well as a lower Ne/O than expected, this may indicate the strong action of the ON and NeNa cycles. We have compared the chemical composition of NGC 6888, G2.4+1.4, RCW 58 and S 308 with the nucleosynthesis predicted by stellar evolution models of massive stars. We find that non-rotational models of stars of initial masses between 25 and 40 M_⊙ seem to reproduce the observed abundance ratios of most of the nebulae.

Key words: ISM: abundances – ISM: H II regions – ISM: bubbles – stars: massive – stars: Wolf-Rayet

1 INTRODUCTION

Ring nebulae are interstellar bubbles of ionised gas that have swept-up the surrounding circumstellar medium after the mass loss episodes experienced by their massive progenitors. They are rather common around Wolf-Rayet (WR) stars and luminous blue variables (LBVs) but are rarely seen around main-sequence O stars. This may depend on the density of the circumstellar material on which they develop (e.g. Nazé et al. 2001). There have been several spectroscopical works devoted to study the chemical composition of ring nebulae around WR stars (e.g. Kwitter 1984; Esteban et al. 1992; Stock et al. 2011) and LBVs (e.g. Smith et al. 1997, 1998). These works have found that some ring nebulae show clear chemical enrichment patterns, in general they are He and N enriched and some of them show some O deficiency, indicating that they are composed by material ejected by the central star. Therefore, a detailed analysis of the chemical composition of stellar ejecta in ring

nebulae would allow us to explore the nucleosynthesis of massive stars, constrain stellar evolution models and the evolutive scenario of the stellar progenitors. Esteban & Vilchez (1992), Esteban et al. (1992) and Mesa-Delgado et al. (2014) compared the abundance pattern of Galactic ejecta ring nebulae with the surface abundances predicted by the evolutionary models of massive stars. These authors found that the He, N and O abundances of the nebulae are consistent with the expected nucleosynthesis for stars with initial masses between 25 and 40 M_⊙ at a given moment of the red supergiant (RSG) phase, prior to the onset of the WR stage. A similar result was obtained by Garnett & Chu (1994) for the ejecta nebula associated to the WR star Br 13 in the Large Magellanic Cloud.

The absence of bright emission lines of C in the optical spectrum of ionised gas has hampered to determine the C abundance in ring nebulae. This is of special importance because C is one of the key elements of the CNO cycle and its abundance should be affected by nucleosynthesis in the H-burning zone. Rodríguez (1999); Moore et al. (2002b) and Mesa-Delgado & Esteban (2010) measured the C II 4267 Å recombination line (hereafter RL) in

* E-mail: cel@iac.es

Table 1. Journal of observations.

Nebula	Ionising Star	Spectral Type ^a	Telescope/ /Spectrograph	RA ^b	DEC ^b	(^o)	PA Grating ^c	Exposure Time (s)
S 308	WR6	WN4	Magellan/MagE	06 53 02.2	−23 53 30	108 ^d	–	1800
RCW 52	CPD−57 3781	O8	Magellan/MagE	10 46 02.5	−58 38 05	28 ^d	–	4400
RCW 58	WR40	WN8	Magellan/MagE	11 06 00.1	−65 32 06	−32 ^d	–	6000
G2.4+1.4	WR102	WO2	Magellan/MagE	17 45 53.9	−26 09 57	−103 ^d	–	6000
			GTC/OSIRIS	17 45 54.4	−26 08 49	4	R1000B	60, 4460
							R2500V	60, 3568
NGC 6888	WR136	WN6	GTC/OSIRIS	20 12 29.6	+38 27 23	66	R1000B	60, 4455
							R2500V	60, 3564
NGC 7635	BD+60 2522	O6.5f	GTC/OSIRIS	23 20 48.5	+61 12 00	13	R1000B	60, 4455
							R2500V	60, 3564

^a Of the ionising star.^b Coordinates of the slit center (J2000.0).^c MagE has a single available grating.^d Parallax angle.

NGC 7635 and Mesa-Delgado et al. (2014) in NGC 6888. In particular, the C^{2+}/H^+ ratios determined by Mesa-Delgado & Esteban (2010), Mesa-Delgado et al. (2014) and Vamvatira-Nakou et al. (2016) led to C abundances substantially higher than those expected by the Galactic C radial abundance gradient, a result that is inconsistent with nucleosynthesis predictions. On the other hand, Mesa-Delgado & Esteban (2010) measured the O II RLs around 4650 Å in an integrated spectrum of NGC 7635 finding that the O^{2+}/H^+ ratio determined from RLs was about 0.6 dex higher than that determined from the far much brighter [O III] collisionally excited lines (hereafter CELs). This is the so-called abundance discrepancy problem and affects virtually to all ionised nebulae. However, the difference found in NGC 7635 is much higher than the values usually found in H II regions (García-Rojas & Esteban 2007).

The aim of this paper is to use high-efficiency spectrographs in large-aperture telescopes in order to reassess the chemical abundances of several of the brightest and more interesting ring nebulae surrounding Galactic WR and O-type massive stars. The use of this state-of-the-art instrumentation would permit to measure C II and/or O II RLs in some of the objects and therefore to derive the C/H ratio and explore the behavior of the abundance discrepancy problem in ring nebulae. Another aim of the work is to compare the abundance pattern of the stellar ejecta objects with predictions of stellar evolution models, applying the same procedure followed by Mesa-Delgado et al. (2014) in order to constrain the mass of their progenitor stars.

The structure of the paper is as follows. In Section 2, we describe the observations and the data reduction procedure. In Section 3, we describe the emission-line measurements and identifications as well as the reddening correction. In Section 4, we present the physical conditions, ionic and total abundances determined for the sample objects, and the abundance discrepancy factors and temperature fluctuations parameter values we obtain for some of the nebulae. In Section 5, we discuss the behavior of the abundance patterns found in the sample nebulae, the presence of shock excitation in localized zones of NGC 6888 and the comparison with stellar evolution models. Finally, in Section 6, we summarize our main conclusions.

2 OBSERVATIONS AND DATA REDUCTION

The observations were performed using two telescopes, one in each hemisphere: the 10.4m Gran Telescopio Canarias (GTC) located at Observatorio del Roque de los Muchachos (La Palma, Spain) and the 6.5 Magellan Clay telescope at Las Campanas Observatory (Chile).

Spectra of NGC 7635, NGC 6888 and G2.4+1.4 were taken with OSIRIS (Optical System for Imaging and low-Intermediate-Resolution Integrated Spectroscopy) spectrograph (Cepa et al. 2000, 2003) attached to the GTC telescope. OSIRIS consists of a mosaic of two Marconi CCD42-82 CCDs each with 2048×4096 pixels and a 74 pixel gap between them. Each pixel has a physical size of $15\mu\text{m}$. We used a binning 2×2 for our observations, giving a plate scale of 0.254 arcsec. OSIRIS was used in long-slit mode. The slit length was 7.4 arcmin and the width was set at 0.8 arcsec. We used two grisms in the OSIRIS observations, R1000B and R2500V. R1000B was used to cover the whole optical spectral range, from 3640 to 7870 Å. R2500V covered from 4430 to 6070 Å and was used to improve the resolution in the spectral zone where [O III] 4363 Å or the RLs of O II around 4650 Å lie. The effective spectral resolution was 6.52 and 2.46 Å for the R1000B and R2500V grisms, respectively. The slit was placed covering the brightest and/or interesting zones of the nebulae. Table 1 shows the coordinates of the centre and position angle (PA) of the slit, and total integration time of the spectra. We selected several apertures in the objects observed with OSIRIS in long-slit mode (NGC 6888, NGC 7635 and G2.4+1.4) in order to extract one-dimensional spectra. These zones were selected attending to their brightness, particular location and the detection of the auroral collisionally excited lines [O III] 4363 Å or [N II] 5755 Å that are used for the determination of electron temperature. In figures 1 and 2 we indicate the position of the areas – apertures – extracted for each object. For example, in the case of NGC 7635, our aperture no. 1 was placed in order to determine the physical conditions and abundances of the neighboring diffuse H II region S 162. The size of the different apertures is indicated in the third to last row of tables 2, 3, 4 and 5. The OSIRIS spectra were wavelength calibrated with Hg-Ar, Ne and Xe lamps. The correction for atmospheric extinction was performed using the average curve for continuous atmospheric extinction at Roque de los Muchachos Observatory. The absolute

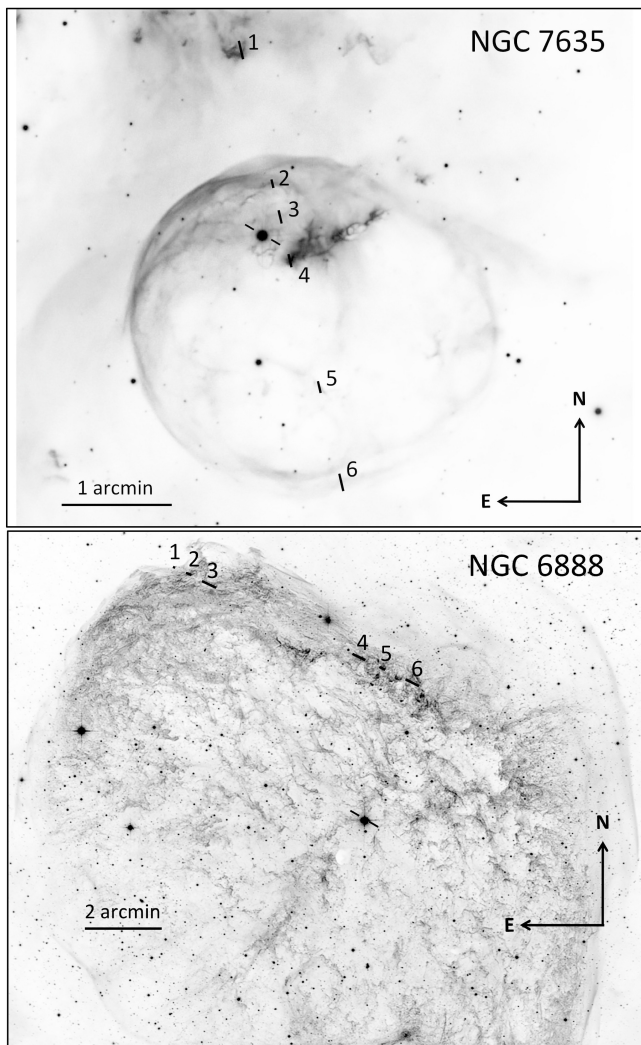


Figure 1. Apertures observed in NGC 7635 and NGC 6888. The image of NGC 7635 is adapted from an original one based on a combination of $H\alpha$, $[O\text{III}]$ and $[S\text{II}]$ emission exposures taken by Josef Pössel and Stefan Binnewies (www.capella-observatory.com). The image of NGC 6888 is adapted from a combination of $H\alpha$ and $[O\text{III}]$ emission exposures taken by Daniel López (IAC/INT). The position of the ionising stars of the nebulae are indicated by a pair of short lines.

flux calibration was achieved by observations of the standard stars BD+33 2642, GD248 (Oke 1990), Hiltner 600 (Massey et al. 1988) and Ross 640 (Oke 1974). We used the IRAF¹TWODSPEC reduction package to perform bias correction, flat-fielding, cosmic-ray rejection, sky emission subtraction, wavelength and flux calibration. We checked the relative flux calibration between the bluest and the reddest wavelengths by calibrating with the different spectrophotometric standards observed in the same night and with each standard itself. The error in the relative flux calibration along the spectral range covered was lower than 3%.

Two half-nights were granted in Las Campanas Observatory (Chile) on 30th January and 13th May 2013 to observe four ring

nebulae of the southern hemisphere. On the one hand, RCW 52 and S 308 were observed during the first night that corresponded to bright time, so the spectroscopic data presented features of scattered moonlight. On the other hand, G2.4 + 1.4 and RCW 58 were observed in the second night during dark time. The observations have provided the deepest spectra available for these objects so far and were obtained using the Magellan Echelle (MagE) spectrograph in the 6.5m Clay Telescope (Marshall et al. 2008). Within the same chip, this instrument provides echelle spectroscopy on the entire optical range (3100 – 10000 Å) with a slit of 10 arcsec long and a fixed plate scale of 0.3 arcsec. The slit width was set to 1.0 arcsec, providing a spectral resolution of about $\lambda/\Delta\lambda \sim 4000$. Each target was observed in a single slit position, placed on the sky along the parallactic angle and covering the brightest areas of the nebulae. The MagE spectra were reduced making use of the ECHELLE package of IRAF, following the typical reduction process: bias subtraction, order tracing, aperture extractions, flat-fielding, wavelength calibration and flux calibration. The final spectra of RCW 58, RCW 52 and S 308 were extracted for areas of about 8-9 arcsec², using most of the slit length. In the case of G2.4 + 1.4, an area of 4 arcsec² was extracted and centered on a bright knot to maximize the signal-to-noise ratio of the final spectra. The wavelength calibration was derived from Th-Ar arcs observed after and before each target. To achieve the flux calibration of the dataset, the spectrophotometric standard star GD 108 (Oke 1990) was observed on 30th January, while GD 108 and EG 274 (Hamuy et al. 1994) were observed on 13th May. Though the seeing was about 0.8 arcsec, the nights were not completely photometric. We applied the same procedure than for the GTC data to estimate the quality of the flux calibration. The error in the relative flux calibration was lower than 3%.

3 LINE INTENSITY MEASUREMENTS

Line fluxes were measured with the SPLIT routine of IRAF by integrating all the flux in the line between two given limits and over the average local continuum. All line fluxes of a given spectrum have been normalized to $H\beta = 100.0$. In general, in the case of GTC data, the lines measured in the spectra taken with the grating 2500V were used instead of those measured with the 1000B in the spectral range between 4430 and 6070 Å. In the case of line blending, we applied a double or multiple Gaussian profile fit procedure using SPLIT routine of IRAF to measure the individual line intensities. Line deblending was especially important in the spectral zone around multiplet 1 of $O\text{II}$ at about 4650 Å. In the case of NGC 6888, where the signal-to-noise ratio of the spectra is much higher and the line profiles better resolved (see Figure 3), we used Starlink DIPSO software for the Gaussian fitting (Howard & Murray 1990) to deblend the lines in the spectral range around 4650 Å. For each single or multiple Gaussian fit, DIPSO yields the fit parameters (centroid, gaussian sigma, flux, FWHM, etc.) and their associated statistical errors. The identification of the lines were obtained following our previous works on spectroscopy of bright Galactic $H\text{II}$ regions (see García-Rojas & Esteban 2007, and references therein).

The reddening coefficient, $c(H\beta)$, was determined from the comparison of the observed flux ratio of the brightest Balmer lines – $H\alpha$, $H\gamma$ and $H\delta$ – with respect to $H\beta$ and the theoretical line ratios computed by Storey & Hummer (1995) for the physical conditions of the nebulae and following an iterative process. We have used the reddening function, $f(\lambda)$, normalized to $H\beta$ derived by Cardelli et al. (1989) and assuming $R_V = 3.1$.

In tables 2, 3, 4 and 5 we include the list of line identifica-

¹ IRAF is distributed by National Optical Astronomy Observatory, which is operated by Association of Universities for Research in Astronomy, under cooperative agreement with the National Science Foundation.

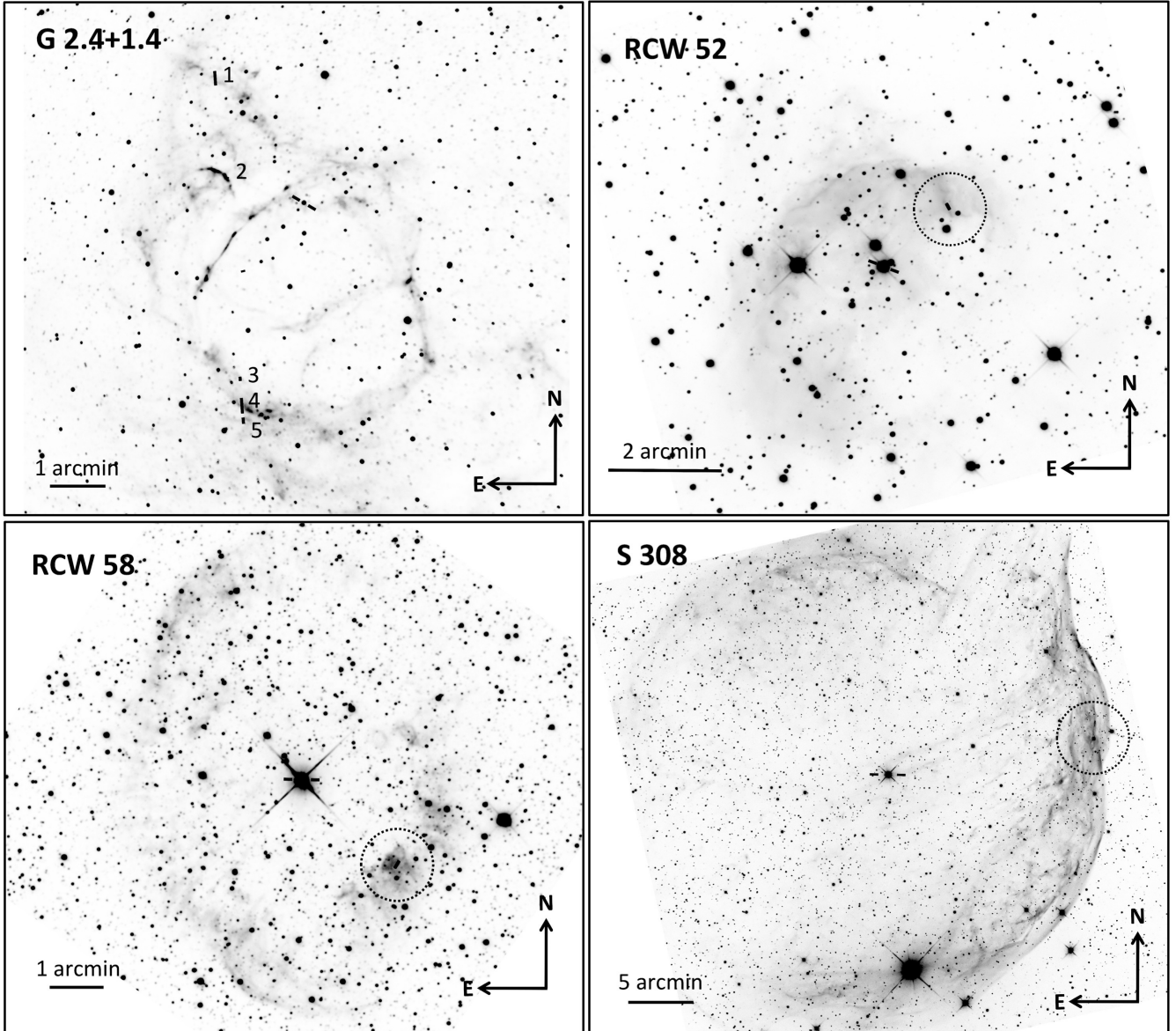


Figure 2. Observed slit positions over G2.4+1.4, RCW 52, RCW 58 and S 308. The centre of the circles drawn over RCW 52, RCW 58 and S 308 indicate the slit positions in these objects. The image of G2.4+1.4 is adapted from an original $H\alpha$ exposure taken with the IAC80 telescope at Observatorio del Teide. The images of RCW 52 and RCW 58 are based on original $H\alpha$ and RGB exposures obtained by Rick Gilbert (Star Shadows Remote Observatory, SSRO). The image of S 308 is adapted from a combination of $H\alpha$ and $[O\text{ III}]$ emission exposures taken by Don Goldman (www.astrodonimaging.com). The position of the ionising stars of the nebulae are indicated by a pair of short lines.

tions – first 3 columns, the reddening function, $f(\lambda)$ – fourth column – and dereddened flux line ratios with respect to $H\beta$ – rest of columns. The quoted line intensity errors include the uncertainties in line flux measurement and error propagation in the reddening coefficient. The 3 last rows of each table include the size, the reddening coefficient and the observed –uncorrected for reddening– integrated $H\beta$ flux, $F(H\beta)$, of each aperture.

4 RESULTS

4.1 Physical Conditions

Physical conditions were calculated making use of the version 1.0.2 of PYNEB (Luridiana et al. 2015) in combination with the atomic data listed in Table 5 of Esteban et al. (2014). PYNEB is an updated and more versatile version of the NEBULAR package of IRAF written in PYTHON language. The density-sensitive emission line ratios we have used are $[S\text{ II}]$ 6717/6731 for all the objects; $[Cl\text{ III}]$ 5518/5538 for several apertures of NGC 7635, NGC 6888 and G2.4+1.4 and $[O\text{ II}]$ 3726/3729 in the case of the higher resolution spectra taken with MagE spectrograph. The electron density is below 300 cm^{-3} in all the objects and apertures except in aperture no. 2 of G2.4+1.4

Table 2. Derredened line intensity ratios with respect to $I(\text{H}\beta) = 100$ for NGC 7635.

λ_0 (Å)	Ion	ID	$f(\lambda)$	$I(\lambda)/I(\text{H}\beta)$					
				A1	A2	A3	A4	A5	A6
3705	He I	25	0.260	–	–	4.1 :	0.64 :	–	–
3712	H I	H15	0.259	–	–	–	0.87 ± 0.32	–	–
3726 ^a	[O II]	1F	0.257	192.7 ± 5.8	91.6 ± 3.8	128.8 ± 5.0	192.9 ± 4.1	162 ± 12	151 ± 11
3729	[O II]	1F							
3750	H I	H12	0.253	2.1 :	1.2 :	1.2 :	2.18 ± 0.15	–	–
3771	H I	H11	0.249	2.46 ± 0.78	3.6 :	3.3 ± 1.1	3.29 ± 0.20	–	–
3798	H I	H10	0.244	4.32 ± 0.95	5.1 :	3.18 ± 0.90	4.41 ± 0.13	–	–
3820	He I	22	0.240	0.67 :	–	–	0.71 ± 0.14	–	–
3835	H I	H9	0.237	8.3 ± 1.7	8.6 ± 2.2	8.6 ± 2.0	6.86 ± 0.21	24.8 ± 7.8	19.9 ± 3.3
3856	Si II	1F	0.233	–	–	–	0.22 :	–	–
3856	O II	12							
3867	He I	20	0.231	0.99 :	6.5 ± 1.1	6.7 ± 1.7	0.93 ± 0.14	–	–
3869	[Ne III]	1F							
3889	He I	2	0.227	15.93 ± 0.69	17.7 ± 1.5	20.6 ± 1.3	14.24 ± 0.35	19.6 ± 3.4	16.6 ± 1.9
3889	H I	H8							
3919	C II	4	0.220	–	–	–	0.54 ± 0.12	–	–
3921	C II	4	0.220	–	–	–	0.86 ± 0.13	–	–
3927	He I	58	0.219	–	–	–	0.248 ± 0.060	–	–
3949	[Fe II]		0.214	–	–	–	0.161 ± 0.041	–	–
3967	[Ne III]	1F	0.211	15.47 ± 0.86	15.8 ± 1.4	16.0 ± 1.1	16.05 ± 0.36	9.3 ± 2.8	6.6 ± 1.3
3970	H I	H7							
3995	N II		0.205	–	1.54 ± 0.61	1.43 ± 0.45	–	–	–
4001	[Cr III]?		0.204	–	–	–	1.65 ± 0.20	–	–
4026	He I	18	0.198	1.57 ± 0.50	1.7 :	1.43 ± 0.45	1.53 ± 0.10	3.3 ± 1.0	–
4069	[S II]	1F	0.189	2.54 ± 0.31	–	–	5.42 ± 0.20	–	–
4076	[S II]	1F	0.187	0.66 ± 0.21	–	–	2.04 ± 0.11	–	–
4102	H I	H6	0.182	25.20 ± 0.81	25.3 ± 0.7	26.9 ± 1.0	25.65 ± 0.53	28.4 ± 1.5	26.7 ± 1.5
4121	He I	16	0.177	–	–	–	0.08 :	–	–
4131	[Fe III]		0.175	–	–	–	0.09 :	–	–
4144	He I	53	0.172	–	–	0.29 :	0.218 ± 0.027	2.0 :	–
4153	O II	19	0.170	–	–	0.31 ± 0.04	–	–	–
4267	C II	6	0.144	–	0.21 :	0.38 :	0.149 ± 0.020	–	–
4340	H I	Hγ	0.127	44.6 ± 1.0	47.3 ± 1.1	48.8 ± 1.2	45.8 ± 0.9	51.6 ± 1.7	49.8 ± 1.3
4363	[O III]	2F	0.121	–	0.70 ± 0.18	0.49 ± 0.15	0.274 ± 0.053	–	–
4388	He I	51	0.115	0.48 ± 0.18	0.41 :	0.51 :	0.404 ± 0.036	–	–
4461	[Ni II]		0.098	–	–	–	0.05 :	–	–
4471	He I	14	0.096	3.34 ± 0.11	3.98 ± 0.23	4.14 ± 0.14	3.13 ± 0.07	3.90 ± 0.40	3.37 ± 0.19
4563	[Mg I]		0.073	0.16 :	–	–	0.047 ± 0.010	–	–
4571	Mg I	1	0.071	0.17 ± 0.04	–	–	0.165 ± 0.012	–	–
4607	[Fe III]	3F	0.062	–	–	–	0.047 ± 0.017	–	–
4621	N II	5	0.059	–	–	–	0.018 :	–	–
4631	N II	5	0.057	0.05 :	0.14 ± 0.05	0.155 ± 0.044	0.041 ± 0.011	–	–
4634	N III	2	0.056	–	–	0.118 ± 0.034	–	–	–
4639	O II	1	0.055	0.10 :	0.379 ± 0.095	0.572 ± 0.086	0.032 ± 0.009	–	–
4641	N III	2							
4642	O II	1	0.054				0.056 ± 0.011		
4643	N II	5							
4649	O II	1	0.052	–	0.340 ± 0.095	0.302 ± 0.073	0.040 ± 0.010	–	–
4651	O II	1							
4658	[Fe III]	3F	0.050	0.05 ± 0.02	0.14 ± 0.05	0.138 ± 0.052	0.385 ± 0.010	–	–
4662	O II	1	0.049	–	0.132 ± 0.050	0.075 ± 0.028	–	–	–
4702	[Fe III]	3F	0.039	–	–	–	0.117 ± 0.012	–	–
4713	He I	12	0.036	0.34 ± 0.05	0.37 ± 0.07	0.39 ± 0.05	0.353 ± 0.015	–	–
4734	[Fe III]	3F	0.031	–	–	–	0.045 ± 0.007	–	–
4755	[Fe III]	3F	0.026	0.62 ± 0.13	–	–	0.081 ± 0.011	–	–
4770	[Fe III]	3F	0.023	–	–	–	0.036 ± 0.012	–	–
4778	[Fe III]	3F	0.021	–	–	–	0.015 :	–	–
4789	[Fe III]		0.018	–	–	–	0.006 ± 0.002	–	–
4793	[Cr III]?		0.017	–	–	–	0.006 :	–	–
4802	[Co II]?		0.015	–	–	–	0.012 :	–	–
4815	[Fe II]	20F	0.012	–	–	0.07 :	0.048 ± 0.010	–	–
4861	H I	Hβ	0.000	100.0 ± 2.1	100.0 ± 2.1	100.0 ± 2.1	100.0 ± 2.0	100.0 ± 2.0	100.0 ± 2.1

Table 2. continued

λ_0 (Å)	Ion	ID	f(λ)	$I(\lambda)/I(H\beta)$					
				A1	A2	A3	A4	A5	A6
4881	[Fe III]	2F	-0.005	–	–	0.07 :	0.146 ± 0.032	–	–
4890	[Fe II]	4F	-0.007	–	–	0.08 ± 0.03	0.018 :	–	–
4905	[Fe II]	20F	-0.011	–	0.09 :	0.09 ± 0.03	–	–	–
4922	He I	48	-0.015	0.94 ± 0.06	1.34 ± 0.11	1.36 ± 0.11	0.867 ± 0.022	1.05 ± 0.22	0.76 ± 0.17
4931	[Fe III]	1F	-0.017	–	–	–	0.018 ± 0.005	–	–
4931	[O III]	1F	–	–	–	–	–	–	–
4959	[O III]	1F	-0.024	21.51 ± 0.44	78.2 ± 1.6	68.0 ± 1.4	22.47 ± 0.45	39.09 ± 0.84	30.37 ± 0.72
4987	[Fe III]	2F	-0.031	–	–	–	0.048 :	–	–
4994	N II	24	-0.033	–	–	0.09 :	0.037 :	–	–
5007	[O III]	1F	-0.036	65.2 ± 1.3	241.6 ± 4.9	204.4 ± 4.1	67.9 ± 1.4	119.3 ± 2.5	93.6 ± 1.9
5016	He I	4	-0.038	2.11 ± 0.07	–	–	1.69 ± 0.11	2.52 ± 0.14	2.35 ± 0.16
5033	[Fe III]	–	-0.042	–	–	–	0.051 ± 0.007	–	–
5035	[Fe II]	4F	-0.043	–	–	–	0.023 ± 0.006	–	–
5041	Si II	5	-0.044	0.15 ± 0.03	0.28 ± 0.06	0.23 ± 0.07	0.131 ± 0.008	–	–
5048	He I	47	-0.046	0.16 ± 0.04	0.20 ± 0.06	0.15 ± 0.05	0.151 ± 0.008	–	–
5056	Si II	5	-0.048	0.19 ± 0.02	0.21 ± 0.04	0.19 ± 0.05	0.362 ± 0.008	–	–
5085	[Fe III]	1F	-0.055	–	–	–	0.012 ± 0.003	–	–
5104	[Ni III]	–	-0.059	–	–	–	0.008 ± 0.003	–	–
5112	[Fe II]	19F	-0.061	–	–	–	0.006 ± 0.002	–	–
5122	C II	12	-0.064	–	–	–	0.006 :	–	–
5125	[Cr III]?	–	-0.065	–	–	–	0.006 :	–	–
5132	[Co II]?	–	-0.066	–	–	–	0.008 :	–	–
5147	O II	28	-0.070	–	–	–	0.030 ± 0.008	–	–
5159	[Fe II]	19F	-0.073	–	–	–	0.055 ± 0.007	–	–
5192	[Ar III]	3F	-0.081	0.04 ± 0.01	–	–	0.036 ± 0.011	–	–
5198	[Ni I]	1F	-0.082	0.30 ± 0.04	–	–	0.326 ± 0.017	–	–
5200	[Ni I]	1F	–	–	–	–	–	–	–
5262	[Fe II]	19F	-0.098	–	–	–	0.026 ± 0.007	–	–
5270	[Fe III]	1F	-0.100	0.07 ± 0.01	0.07 ± 0.02	0.09 ± 0.04	0.224 ± 0.012	–	–
5299	O I	26	-0.107	–	–	–	0.020 ± 0.004	–	–
5334	[Fe II]	19F	-0.115	–	–	–	0.015 :	–	–
5342	C II	17.06	-0.117	–	–	–	0.014 ± 0.004	–	–
5376	[Fe II]	19F	-0.125	–	–	–	0.009 ± 0.004	–	–
5412	[Fe III]	1F	-0.136	–	–	–	0.018 ± 0.003	–	–
5433	[Fe II]	18F	-0.139	–	–	–	0.020 ± 0.005	–	–
5455	[Cr III]?	2F	-0.143	–	–	–	0.023 ± 0.005	–	–
5496	[Fe II]	17F	-0.150	–	–	0.03 :	0.012 :	–	–
5513	O I	25	-0.153	–	–	–	0.031 ± 0.007	–	–
5518	[Cl III]	1F	-0.154	0.40 ± 0.03	0.65 ± 0.06	0.64 ± 0.05	0.413 ± 0.011	0.58 ± 0.09	0.52 ± 0.13
5527	[Fe II]	17F	-0.156	–	–	–	0.011 :	–	–
5538	[Cl III]	1F	-0.158	0.30 ± 0.02	0.47 ± 0.07	0.42 ± 0.05	0.500 ± 0.017	0.38 ± 0.05	0.27 ± 0.07
5555	O I	24	-0.160	–	–	–	0.019 :	–	–
5640	[Fe I] ?	–	-0.175	–	–	–	0.015 :	–	–
5667	N II	3	-0.180	0.04 :	0.07 :	0.04 ± 0.01	0.028 ± 0.006	–	–
5676	N II	3	-0.181	–	–	–	0.013 ± 0.003	–	–
5680	N II	3	-0.182	0.03 :	0.09 :	0.05 :	0.042 ± 0.011	–	–
5711	N II	3	-0.187	–	–	–	0.011 ± 0.003	–	–
5713	[Fe II]	–	-0.187	–	–	0.05 :	–	–	–
5740	Si III	4	-0.192	–	0.10 ± 0.03	0.18 ± 0.03	0.013 ± 0.004	–	–
5755	[N II]	3F	-0.194	0.72 ± 0.04	0.26 ± 0.05	0.35 ± 0.05	1.442 ± 0.031	0.50 ± 0.08	0.47 ± 0.08
5876	He I	11	-0.215	11.24 ± 0.27	15.58 ± 0.34	14.01 ± 0.37	10.19 ± 0.21	13.46 ± 0.57	12.45 ± 0.41
5932	N II	28	-0.224	–	–	–	0.027 ± 0.008	–	–
5942	N II	28	-0.225	–	–	–	0.030 ± 0.008	–	–
5958	O I	23	-0.228	–	–	–	0.099 ± 0.010	–	–
5979	Si II	4	-0.231	0.06 ± 0.01	–	–	0.117 ± 0.016	–	–
6046	O I	22	-0.242	–	–	–	0.076 ± 0.015	–	–
6300	[O I]	1F	-0.282	0.84 ± 0.11	–	–	2.118 ± 0.090	–	–
6312	[S III]	3F	-0.283	0.87 ± 0.09	1.58 ± 0.12	1.49 ± 0.16	1.907 ± 0.084	0.71 ± 0.11	0.67 ± 0.17
6347	Si II	4	-0.289	0.16 ± 0.05	0.21 :	–	0.272 ± 0.049	–	–
6364	[O I]	1F	-0.291	0.29 ± 0.06	–	–	0.758 ± 0.078	–	–
6371	Si II	2	-0.292	0.06 :	–	–	0.106 ± 0.015	–	–

Table 2. continued

λ_0 (Å)	Ion	ID	f(λ)	$I(\lambda)/I(H\beta)$					
				A1	A2	A3	A4	A5	A6
6548	[N II]	1F	-0.318	28.9 ± 1.1	10.32 ± 0.76	13.49 ± 0.43	40.34 ± 0.90	19.8 ± 1.1	20.16 ± 0.78
6563	H I	H α	-0.320	281.5 ± 7.8	292.0 ± 6.8	306.9 ± 9.9	287.7 ± 6.2	325 ± 18	309 ± 11
6583	[N II]	1F	-0.323	85.9 ± 2.4	32.43 ± 0.78	41.3 ± 1.3	123.2 ± 2.7	59.9 ± 3.4	59.7 ± 2.2
6678	He I	46	-0.336	3.13 ± 0.09	4.72 ± 0.15	4.04 ± 0.17	2.860 ± 0.064	3.64 ± 0.23	3.26 ± 0.21
6716	[S II]	2F	-0.342	26.06 ± 0.74	6.67 ± 0.17	9.19 ± 0.32	13.74 ± 0.30	13.23 ± 0.79	15.84 ± 0.64
6731	[S II]	2F	-0.344	27.12 ± 0.77	5.23 ± 0.14	6.96 ± 0.25	18.83 ± 0.41	10.94 ± 0.67	11.36 ± 0.47
7002	O I	21	-0.379	–	–	–	0.039 ± 0.012	–	–
7035	[Co II]?		-0.384	–	–	–	0.025 :	–	–
7065	He I	10	-0.387	3.52 ± 0.14	3.88 ± 0.11	3.66 ± 0.17	4.178 ± 0.097	3.53 ± 0.33	3.27 ± 0.19
7136	[Ar III]	1F	-0.396	7.42 ± 0.24	13.92 ± 0.38	11.91 ± 0.45	8.23 ± 0.18	9.81 ± 0.72	8.03 ± 0.37
7155	[Fe II]	14F	-0.399	–	–	–	0.065 ± 0.024	–	–
7233	[Cr II]?		-0.408	–	1.42 ± 0.48	1.02 ± 0.21	0.385 ± 0.097	–	–
7254	O I	20	-0.411	–	–	–	0.16 :	–	–
7281	He I	45	-0.414	0.39 :	0.55 :	0.28 ± 0.09	0.475 ± 0.049	1.07 ± 0.29	–
7298	He I	1/9	-0.416	–	–	–	0.027 :	–	–
7318 ^b	[O II]	2F	-0.418	1.90 ± 0.41	0.95 ± 0.23	1.04 ± 0.16	7.92 ± 0.18	1.33 ± 0.33	0.84 ± 0.18
7320	[O II]								
7330 ^c	[O II]	2F	-0.420	2.18 ± 0.27	1.97 ± 0.34	2.04 ± 0.22	7.97 ± 0.18	3.49 ± 0.41	3.17 ± 0.32
7331	[O II]								
7428	[Fe II]		-0.431	–	–	–	0.180 ± 0.037	–	–
7468	N I	3	-0.436	–	–	–	0.032 :	–	–
7751	[Ar III]	2F	-0.467	1.87 ± 0.41	2.52 ± 0.38	2.12 ± 0.24	1.682 ± 0.057	2.29 ± 0.28	–
7774	O I	1	-0.469	–	–	–	0.07 :	–	–
7816	He I	1/7	-0.473	–	–	–	0.11 :	–	–
Aperture size (arcsec ²)				10.4 × 0.8	4.8 × 0.8	7.4 × 0.8	7.4 × 0.8	6.6 × 0.8	9.7 × 0.8
$c(H\beta)$				0.90 ± 0.03	0.70 ± 0.02	0.89 ± 0.03	0.99 ± 0.02	1.11 ± 0.07	1.10 ± 0.04
$F(H\beta)$ (10^{-14} erg cm ⁻² s ⁻¹)				3.54 ± 0.07	1.80 ± 0.04	2.27 ± 0.05	22.3 ± 0.4	0.41 ± 0.01	0.66 ± 0.01

^a Blend of [O II] 3726 and 3729 Å lines.

^b Blend of [O II] 7318 and 7320 Å lines and affected by sky emission.

^c Blend of [O II] 7330 and 7331 Å lines and affected by sky emission.

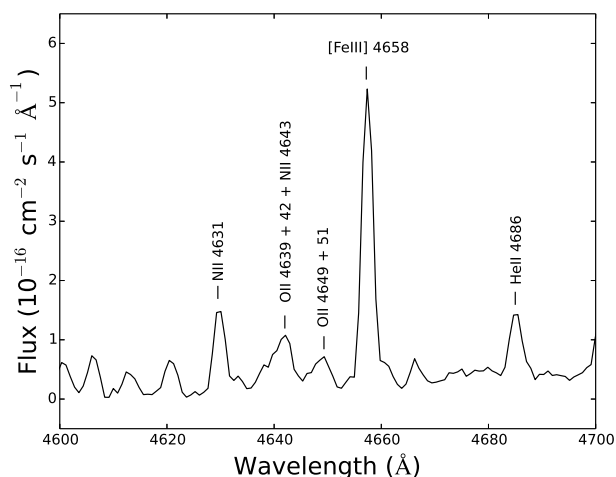


Figure 3. Section of the OSIRIS spectrum of aperture no. 6 of NGC 6888 –uncorrected for reddening– showing the recombination lines of multiplet 1 of O II about 4650 Å and other nearby emission lines.

and aperture no. 4 of NGC 7635 where the values are 1200 and 2500 cm⁻³, respectively. We have assumed $n_e([S II])$ as representative for all the apertures and objects. The temperature-sensitive

emission line ratios we have used are [N II] 5755/(6548+6584) for all objects; [S II] (4069+4076)/(6717+6731) for a single aperture of NGC 7635 and G2.4+1.4; [O III] 4363/(4959+5007) for NGC 6888, S 308 and several apertures of NGC 7635 and G2.4+1.4; [S III] 6312/(9069+9532) for S 308 and finally [Ar III] 5192/(7136+7751) for several apertures of NGC 7635, NGC 6888 and G2.4+1.4. The temperature-sensitive emission line ratio [O II] (7319+7330)/(3726+3729) was not used due to the strong contamination by sky emission features.

Temperatures and densities were determined using an iterative procedure. Firstly, we assumed an initial T_e of 10,000 K to determine n_e and this last value was used to calculate T_e . We assumed a two-zone approximation for the nebula estimating the representative values of the electron temperature for the zones where low and high-ionisation potential ions are present, $T_e(\text{low})$ and $T_e(\text{high})$. In all the cases, $T_e([N II])$ was taken as representative of $T_e(\text{low})$. For $T_e(\text{high})$, the weighted average of $T_e([O III])$ and $T_e([Ar III])$ – or $T_e([S III])$ when available – was considered. For RCW 52 and RCW 58 and some apertures of NGC 7635 and G2.4+1.4, the [O III] 4363 Å line was not detected and we assumed $T_e(\text{high}) = T_e(\text{low}) = T_e([N II])$. The physical conditions of the different apertures and nebulae are presented in tables 6, 7, 8 and 9.

In general, the values of n_e and T_e we obtain are consistent with previous determinations. In the case of NGC 7635, most of the areas of the bubble show densities between 100-200 cm⁻³ but the aperture corresponding to S 162 and the bright knot at the south-west of the ionising star – aperture no. 4 – show larger values of

Table 3. Derredened line intensity ratios with respect to $I(\text{H}\beta) = 100$ for NGC 6888.

λ_0 (Å)	Ion	ID	$f(\lambda)$	A1	A2	A3	A4	A5	A6
3705	He I	25	0.260		–	–	2.5 :	–	–
3726 ^a	[O II]	1F	0.257	256.4 ± 5.3	124.1 ± 5.9	93.9 ± 5.0	45.4 ± 4.6	42.6 ± 2.2	50.4 ± 4.7
3729	[O II]	1F							
3750	H I	H12	0.253	–	1.7 :	1.7 :	1.6 :	1.66 ± 0.51	2.1 :
3771	H I	H11	0.249	–	3.6 ± 1.1	3.1 :	3.3 ± 1.2	3.33 ± 0.70	3.6 :
3798	H I	H10	0.244	–	3.77 ± 0.84	3.7 :	4.0 ± 1.4	3.71 ± 0.77	4.3 ± 1.6
3820	He I	22	0.240	–	1.85 ± 0.53	1.5 :	2.6 :	2.8 ± 1.0	2.7 :
3835	H I	H9	0.237	44 ± 12	10.44 ± 0.92	10.2 ± 1.2	9.4 ± 2.2	9.49 ± 0.83	9.1 ± 1.9
3867	He I	20	0.231	47.0 ± 7.0	9.1 ± 1.1	6.68 ± 0.60	15.2 ± 1.9	14.7 ± 1.1	14.3 ± 1.6
3869	[Ne III]	1F							
3889	He I	5	0.227	17.8 ± 5.8	22.0 ± 1.3	24.2 ± 1.1	27.2 ± 2.0	26.9 ± 1.3	28.2 ± 2.0
3889	H I	H8							
3967	[Ne III]	1F	0.211	31 ± 10	19.35 ± 0.83	18.4 ± 1.2	19.9 ± 2.3	20.2 ± 1.6	22.0 ± 1.0
3970	H I	H7							
4026	He I	18	0.198	–	3.63 ± 0.46	4.53 ± 0.74	4.04 ± 0.85	3.69 ± 0.55	3.77 ± 0.40
4069	[S II]	1F	0.189	–	1.0 :	0.875 :	2.2 :	1.9 :	1.39 ± 0.41
4076	[S II]	1F	0.187	–	0.28 :	–	–	–	–
4102	H I	H6	0.182	25.7 ± 5.4	27.45 ± 0.82	28.4 ± 1.0	26.9 ± 1.3	27.2 ± 1.1	27.00 ± 0.82
4121	He I	16	0.177	–	0.94 ± 0.29	0.312 :	–	–	0.38 :
4144	He I	53	0.172	–	–	0.45 ± 0.17	–	–	–
4267	C II	6	0.144	–	0.19 :	0.16 :	0.35 :	0.26 :	0.23 :
4317	O II	2	0.132	–	–	–	–	0.87 :	0.70 :
4340	H I	H γ	0.127	47.0 ± 2.2	47.7 ± 1.1	47.0 ± 1.3	49.2 ± 1.7	50.2 ± 1.3	49.0 ± 1.3
4363	[O III]	2F	0.121	21.9 ± 2.3	2.62 ± 0.22	0.93 ± 0.20	1.67 ± 0.51	1.61 ± 0.29	1.37 ± 0.39
4388	He I	51	0.115	–	0.76 ± 0.12	0.96 ± 0.29	0.78 :	0.84 ± 0.19	0.84 ± 0.21
4471	He I	14	0.096	3.4 :	5.88 ± 0.18	7.09 ± 0.26	8.73 ± 0.91	8.50 ± 0.37	8.82 ± 0.40
4596	O II	15	0.065	–	0.089 ± 0.018	–	–	–	–
4601	N II	5	0.064	–	0.077 ± 0.020	0.083 ± 0.023	0.112 ± 0.028	0.148 ± 0.041	0.122 ± 0.025
4607	[Fe III]	3F	0.062	–	0.132 ± 0.020	0.195 ± 0.039	0.178 ± 0.039	0.173 ± 0.035	0.137 ± 0.026
4613	N II	5	0.061	–	0.134 ± 0.043	0.088 ± 0.028	0.148 ± 0.034	0.146 ± 0.040	0.117 ± 0.026
4621	N II	5	0.059	–	0.130 ± 0.036	0.156 ± 0.058	0.225 ± 0.042	0.219 ± 0.031	0.189 ± 0.035
4631	N II	5	0.057	–	0.235 ± 0.041	0.313 ± 0.033	0.44 ± 0.14	0.477 ± 0.066	0.426 ± 0.046
4639	O II	1	0.055	–	0.096 ± 0.032	0.098 ± 0.029	0.071 ± 0.021	0.116 ± 0.035	0.089 ± 0.032
4641	N III	2							
4642	O II	1	0.054	–	0.152 ± 0.030	0.180 ± 0.036	0.103 ± 0.021	0.168 ± 0.034	0.095 :
4643	N II	5	0.054	–	–	–	0.206 ± 0.031	0.334 ± 0.051	0.290 ± 0.044
4647	C III ?						–	–	0.078 ± 0.023
4649	O II	1	0.052	–	0.22 :	0.107 ± 0.038	0.195 ± 0.058	0.186 ± 0.045	0.166 ± 0.025
4651	O II	1							
4658	[Fe III]	3F	0.050	6.0 ± 1.8	1.11 ± 0.14	1.835 ± 0.099	1.87 ± 0.10	1.85 ± 0.26	1.430 ± 0.060
4662	O II	1	0.049	–	0.413 ± 0.083	0.406 ± 0.082	0.119 ± 0.042	0.118 ± 0.041	0.090 ± 0.027
4667	[Fe III]	3F	0.048	–	–	–	0.08 :	0.123 ± 0.037	0.098 ± 0.029
4674	O II	1	0.043	–	–	–	–	0.073 ± 0.029	–
4686	He II	3.4	0.043	–	–	0.167 ± 0.038	0.398 ± 0.073	0.33 ± 0.10	0.313 ± 0.069
4702	[Fe III]	3F	0.039	–	0.224 ± 0.043	0.422 ± 0.066	0.403 ± 0.083	0.378 ± 0.077	0.299 ± 0.063
4713	He I	12	0.036	–	–	0.617 ± 0.056	0.675 ± 0.069	0.72 ± 0.11	0.679 ± 0.060
4728	[Fe II]	4F	0.031	–	–	–	0.054 ± 0.024	0.032 ± 0.016	0.060 ± 0.021
4734	[Fe III]	3F	0.031	–	0.09 :	0.122 ± 0.034	0.117 ± 0.047	0.095 ± 0.029	0.083 ± 0.025
4755	[Fe III]	3F	0.026	–	0.133 ± 0.044	0.233 ± 0.054	0.228 ± 0.071	0.26 :	0.22 :
4770	[Fe III]	3F	0.023	–	–	0.110 :	–	–	–
4861	H I	H β	0.000	100.0 ± 2.2	100.0 ± 2.0	100.0 ± 2.0	100.0 ± 2.1	100.0 ± 2.1	100.0 ± 2.0
4881	[Fe III]	3F	-0.005	–	0.280 ± 0.038	0.490 ± 0.069	0.350 ± 0.061	0.47 :	0.391 ± 0.094
4922	He I	48	-0.015	0.72 :	1.84 ± 0.11	2.198 ± 0.090	2.47 ± 0.17	2.31 ± 0.33	2.35 ± 0.18
4959	[O III]	1F	-0.024	238.7 ± 5.0	67.9 ± 1.4	47.77 ± 0.99	83.9 ± 1.7	82.9 ± 1.7	81.3 ± 1.7
4986	[Fe III]	3F	-0.031	0.97 :	0.662 ± 0.099	0.87 ± 0.14	1.11 ± 0.23	1.07 ± 0.21	1.02 ± 0.21
4987	N II	24	-0.033						
4994	N II	24	-0.033	–	0.15 :	0.169 :	0.17 :	0.15 :	0.18 :
5007	[O III]	1F	-0.036	703 ± 14	199.9 ± 4.1	143.2 ± 3.0	247.7 ± 5.0	253.2 ± 5.2	242.9 ± 4.9
5016	He I	4	-0.038	2.28 ± 0.63	3.62 ± 0.18	4.30 ± 0.16	3.92 ± 0.19	4.49 ± 0.22	4.43 ± 0.22
5041	Si II	5	-0.044	–	0.195 ± 0.044	0.214 ± 0.051	0.289 ± 0.062	0.331 ± 0.086	0.294 ± 0.042
5045	N II	4	-0.045	–	–	0.116 ± 0.029	–	0.108 ± 0.038	0.074 ± 0.029
5048	He I	47	-0.046	–	0.336 ± 0.065	0.266 ± 0.053	0.234 ± 0.065	0.255 ± 0.072	0.248 ± 0.038
5056	Si II	5	-0.048	–	0.168 ± 0.042	0.138 ± 0.031	0.10 :	0.145 ± 0.033	0.172 ± 0.043

Table 3. continued

λ_0 (Å)	Ion	ID	$f(\lambda)$	A1	A2	$I(\lambda)/I(H\beta)$				A6
						A3	A4	A5		
5159	[Fe II]	19F	-0.073	–	–	0.118 ± 0.034	–	–	–	–
5192	[Ar III]	3F	-0.081	–	$0.06 :$	$0.074 :$	$0.05 :$	0.045 ± 0.013	$0.058 :$	–
5270	[Fe III]	1F	-0.100	–	0.498 ± 0.056	0.920 ± 0.073	0.755 ± 0.053	0.842 ± 0.063	0.644 ± 0.054	–
5412	[Fe III]	1F	-0.134	–	$0.08 :$	0.130 ± 0.026	0.111 ± 0.033	0.089 ± 0.028	$0.074 :$	–
5412	He II	4.7								
5518	[Cl III]	1F	-0.154	1.30 ± 0.45	0.495 ± 0.055	0.472 ± 0.050	0.492 ± 0.043	0.542 ± 0.032	0.529 ± 0.053	–
5538	[Cl III]	1F	-0.158	0.482 ± 0.061	0.347 ± 0.063	0.292 ± 0.025	0.348 ± 0.042	0.406 ± 0.036	0.397 ± 0.058	–
5667	N II	3	-0.180	–	0.140 ± 0.026	0.197 ± 0.029	0.238 ± 0.046	0.275 ± 0.028	0.227 ± 0.069	–
5676	N II	3	-0.181	–	$0.07 :$	0.107 ± 0.025	0.084 ± 0.029	0.109 ± 0.043	0.083 ± 0.022	–
5680	N II	3	-0.182	–	0.158 ± 0.032	0.261 ± 0.025	0.276 ± 0.042	0.363 ± 0.038	0.297 ± 0.037	–
5686	N II	3	-0.183	–	$0.06 :$	0.076 ± 0.020	0.049 ± 0.018	0.084 ± 0.017	–	–
5711	N II	3	-0.187	–	–	$0.074 :$	0.095 ± 0.035	0.109 ± 0.027	–	–
5755	[N II]	3F	-0.194	0.48 ± 0.14	2.088 ± 0.062	2.63 ± 0.10	1.285 ± 0.046	1.344 ± 0.092	1.329 ± 0.067	–
5876	He I	11	-0.215	14.25 ± 0.88	19.68 ± 0.56	23.73 ± 0.86	24.57 ± 0.61	23.6 ± 1.8	25.78 ± 0.65	–
5932	N II	28	-0.227	–	–	–	–	–	0.404 ± 0.077	–
5952	N II	28	-0.283	–	–	–	–	–	0.32 ± 0.12	–
6312	[S III]	3F	-0.283	–	1.32 ± 0.14	0.97 ± 0.12	1.68 ± 0.17	1.98 ± 0.12	1.83 ± 0.11	–
6548	[N II]	1F	-0.318	23.76 ± 0.54	111.3 ± 4.0	130.6 ± 6.3	39.4 ± 1.2	42.3 ± 1.5	41.8 ± 1.2	–
6563	H I	H α	-0.320	285.4 ± 6.0	298 ± 11	308 ± 19	301.5 ± 9.1	306 ± 11	301.6 ± 9.0	–
6583	[N II]	1F	-0.323	69.4 ± 1.6	340 ± 12	397 ± 19	119.2 ± 3.6	131.8 ± 4.8	130.3 ± 3.9	–
6678	He I	46	-0.336	2.65 ± 0.42	5.45 ± 0.22	6.59 ± 0.34	6.69 ± 0.26	7.03 ± 0.35	6.95 ± 0.43	–
6716	[S II]	2F	-0.342	21.18 ± 0.77	15.84 ± 0.61	13.49 ± 0.70	5.42 ± 0.29	5.19 ± 0.22	5.12 ± 0.34	–
6731	[S II]	2F	-0.344	14.61 ± 0.66	13.98 ± 0.54	11.40 ± 0.60	4.25 ± 0.21	4.23 ± 0.22	4.15 ± 0.28	–
7065	He I	10	-0.387	2.56 ± 0.46	3.89 ± 0.20	4.18 ± 0.25	3.86 ± 0.39	4.13 ± 0.33	4.19 ± 0.50	–
7136	[Ar III]	1F	-0.396	14.45 ± 0.53	12.25 ± 0.51	12.64 ± 0.74	14.88 ± 0.63	15.51 ± 0.75	15.22 ± 0.73	–
7281	He I	45	-0.414	–	0.81 ± 0.13	–	–	–	–	–
7318 ^b	[O II]	2F	-0.418	2.75 ± 0.50	1.16 ± 0.18	0.84 ± 0.23	–	–	–	–
7320	[O II]	2F								
7330 ^c	[O II]	2F	-0.420	2.02 ± 0.51	1.01 ± 0.16	0.77 ± 0.19	–	–	–	–
7331	[O II]	2F								
7751	[Ar III]	2F	-0.467	3.61 ± 0.47	2.46 ± 0.26	2.98 ± 0.50	6.5 ± 1.4	6.38 ± 0.94	6.7 ± 1.2	–
Aperture size (arcsec ²)				3.8×0.8	8.9×0.8	24.1×0.8	21.6×0.8	10.2×0.8	22.9×0.8	–
$c(H\beta)$				0.93 ± 0.01	0.88 ± 0.04	0.77 ± 0.06	0.63 ± 0.03	0.61 ± 0.04	0.62 ± 0.03	–
$F(H\beta)$ (10^{-14} erg cm ⁻² s ⁻¹)				0.076 ± 0.002	1.84 ± 0.04	3.88 ± 0.08	6.47 ± 0.13	3.97 ± 0.08	9.71 ± 0.19	–

^a Blend of [O II] 3726 and 3729 Å lines.

^b Blend of [O II] 7318 and 7320 Å lines and affected by sky emission.

^c Blend of [O II] 7330 and 7331 Å lines and affected by sky emission.

n_e . Rodríguez (1999), Moore et al. (2002b) and Mesa-Delgado & Esteban (2010) obtained densities of several thousands cm⁻³ and values of $T_e([N II])$ between 8000 and 9000 K for the knots at the southwest of the ionising star, consistent with the $n_e \approx 2500$ cm⁻³ and $T_e([N II]) = 9080$ K we obtain for our aperture no. 4. For the north edge of the bubble, Moore et al. (2002b) and Mesa-Delgado & Esteban (2010) obtain values of the physical conditions very similar to the ones we derive for apertures no. 2 and 3.

Fernández-Martín et al. (2012) and Reyes-Pérez et al. (2015) observed zones at the north of NGC 6888 not far from our apertures no. 2 and 3 – their Zone X1 and Position A, respectively. Those authors find very similar n_e and $T_e([N II])$ values but the $T_e([O III])$ obtained by Fernández-Martín et al. (2012) is much lower than ours. They found $T_e([O III]) = 6350$ K, and we obtain temperatures between 9960 and 12,650 K. This large difference can be explained attending to the fact that Fernández-Martín et al. (2012) cannot compute directly $T_e([O III])$. Their [O III] 4363 Å line is blended with the sky feature of Hg I 4358 Å, so their $T_e([O III])$ determinations are based on the application of empirical calibrations, that may be appropriate when using integrated spectra of a nebula but of doubtful application for individual apertures covering a small

fraction of it. On the other hand, Mesa-Delgado et al. (2014) and Reyes-Pérez et al. (2015) observed zones rather close to our aperture no. 6 of NGC 6888 – position B of Reyes-Pérez et al. (2015). The densities are consistent with our values in all cases as well as the $T_e([O III])$ determined by Mesa-Delgado et al. (2014), however, the $T_e([N II])$ determined by Reyes-Pérez et al. (2015) is about 3000 K higher. One of the most interesting result of our study is the finding of a very high value of $T_e([O III]) = 19,000$ K – in aperture no. 1 of NGC 6888. The auroral [O III] 4343 Å line has a rather high signal-to-noise ratio in this zone (see Figure 4), so the determination is highly confident. In her PhD Thesis, P. Mitra reported the detection of very high values of $T_e([O III])$ in rather low signal-to-noise spectra of peripheral zones of NGC 6888 (Mitra 1991). In her slit position NO3-W, at the rim of the bubble – rather close to our aperture no. 1 – Mitra obtains $T_e([O III]) \approx 50,000$ K. Dufour (1989) interprets that such high values of the temperature cannot be produced by photoionisation but may be explained by shock models with velocities of about 100 km⁻¹ and incomplete recombination regions of the kind proposed by Raymond et al. (1988) for the Cygnus Loop. We will further discuss the characteristics of this particular spectrum in Section 5.2.

Table 4. Derredened line intensity ratios with respect to $I(\text{H}\beta) = 100$ for G2.4+1.4.

λ_0 (Å)	Ion	ID	$f(\lambda)$	A1	A2	$I(\lambda)/I(\text{H}\beta)$ A3	A4	A5
3726.03 ^a	[O II]	1F	0.257	184 ± 46	115.7 ± 6.2	219 :	96 ± 27	208 ± 62
3728.82	[O II]	1F	0.256	–	92.7 ± 5.8	–	–	–
3835.39	H I	H9	0.237	–	8.6 ± 2.8	–	–	–
3867.49	He I	20	0.230	39 :	67.9 ± 5.9	–	57 ± 13	54 :
3868.75	[Ne III]	1F	–	–	–	–	–	–
3888.65	He I	5	0.227	–	16.7 ± 3.4	–	12 :	–
3889.05	H I	H8	–	–	–	–	–	–
3967.46	[Ne III]	1F	0.211	45 ± 12	15.7 ± 1.8	–	34 ± 12	40 :
3970.07	H I	H7	0.210	–	15.0 ± 2.4	–	–	–
4068.6	[S II]	1F	0.189	–	11.3 ± 2.6	–	–	–
4076.35	[S II]	1F	0.187	–	4.7 ± 1.5	–	–	–
4101.74	H I	H6	0.182	21 :	24.6 ± 2.7	–	21.4 ± 5.9	19 :
4267.15	C II	6	0.144	–	–	–	10.8 ± 3.2	–
4340.47	H I	Hy	0.127	38.8 ± 6.6	46.3 ± 2.2	40 ± 14	43.8 ± 3.7	46 ± 11
4363.21	[O III]	2F	0.121	–	3.9 ± 1.1	–	5.1 ± 1.8	12 :
4471.09	He I	14	0.096	9.7 :	3.65 ± 0.92	–	4.6 :	7.4 :
4658.1	[Fe III]	3F	0.050	–	4.06 ± 0.34	–	–	–
4685.71	He II	3.4	0.043	19.2 ± 3.0	35.0 ± 1.2	43.5 ± 6.1	30.7 ± 1.8	15.5 ± 2.9
4711.37	[Ar IV]	1F	0.037	–	1.43 ± 0.27	–	–	–
4713.14	He I	12	0.036	–	–	–	2.8 :	4.8 :
4740.16	[Ar IV]	1F	0.030	–	0.74 :	–	–	–
4861.33	H I	H β	0.000	100.0 ± 3.2	100.0 ± 2.6	100.0 ± 3.5	100.0 ± 2.2	100.0 ± 3.9
4881	[Fe III]	3F	-0.005	–	0.93 :	–	–	–
4958.91	[O III]	1F	-0.024	186.1 ± 4.6	176.5 ± 3.7	133.9 ± 5.6	201.7 ± 4.3	190.5 ± 4.8
5006.84	[O III]	1F	-0.036	567 ± 12	541 ± 11	428.5 ± 9.8	611 ± 13	586 ± 12
5015.68	He I	4	-0.038	–	1.94 :	–	–	–
5411.52	He II	4.7	-0.133	–	2.93 ± 0.42	–	1.17 ± 0.32	–
5412	[Fe III]	1F	–	–	–	–	–	–
5517.71	[Cl III]	1F	-0.154	0.65 :	0.79 ± 0.27	–	1.1 :	–
5537.88	[Cl III]	1F	-0.158	3.26 ± 0.70	0.60 :	–	1.0 :	–
5754.64	[N II]	3F	-0.194	2.03 ± 0.42	1.83 ± 0.19	3.05 ± 0.96	1.27 ± 0.39	1.72 ± 0.43
5875.64	He I	11	-0.215	9.09 ± 0.63	11.80 ± 0.78	8.8 ± 1.8	11.35 ± 0.60	13.9 ± 1.8
6312.1	[S III]	3F	-0.283	–	2.10 ± 0.27	–	1.7 :	–
6548.03	[N II]	1F	-0.318	70.3 ± 2.2	52.1 ± 1.6	52.2 ± 1.7	29.3 ± 1.1	58.6 ± 1.9
6562.82	H I	H α	-0.320	281.1 ± 8.4	283.6 ± 8.5	286.7 ± 7.1	277.2 ± 9.9	288.4 ± 7.3
6583.41	[N II]	1F	-0.323	192.4 ± 5.8	162.5 ± 4.9	110.1 ± 2.8	77.5 ± 2.8	155.4 ± 4.0
6678.15	He I	46	-0.336	2.12 ± 0.57	3.15 ± 0.26	2.144 :	2.82 ± 0.25	2.71 ± 0.57
6716.47	[S II]	2F	-0.342	53.9 ± 1.8	44.7 ± 1.6	32.9 ± 1.1	23.70 ± 0.90	43.6 ± 1.3
6730.85	[S II]	2F	-0.344	41.7 ± 1.4	54.3 ± 1.8	26.7 ± 1.1	18.06 ± 0.70	33.3 ± 1.0
7065.28	He I	10	-0.387	1.31 ± 0.48	2.17 ± 0.22	–	1.60 ± 0.26	2.02 ± 0.47
7135.78	[Ar III]	1F	-0.396	21.10 ± 0.83	20.25 ± 0.87	13.07 ± 0.63	17.99 ± 0.77	19.36 ± 0.65
7318.39 ^b	[O II]	2F	-0.418	–	2.67 ± 0.28	–	–	–
7319.99	[O II]	2F	–	–	–	–	–	–
7329.66 ^c	[O II]	2F	-0.420	–	5.50 ± 0.49	–	–	–
7330.73	[O II]	2F	–	–	–	–	–	–
9068.90	[S III]	1F	-0.585	–	55.6 ± 2.7	–	–	–
9530.60	[S III]	1F	-0.618	–	122.8 ± 6.6	–	–	–
Aperture size (arcsec ²)				15.5 × 0.8	4.0 × 1.0	4.6 × 0.8	16.8 × 0.8	6.6 × 0.8
$c(\text{H}\beta)$				1.85 ± 0.03	2.09 ± 0.03	2.00 ± 0.02	1.99 ± 0.04	1.95 ± 0.02
$F(\text{H}\beta)$ (10 ⁻¹⁵ erg cm ⁻² s ⁻¹)				2.15 ± 0.07	1.12 ± 0.03	0.37 ± 0.01	3.98 ± 0.09	0.98 ± 0.04

^a Blend of [O II] 3726 and 3729 Å lines.

^b Blend of [O II] 7318 and 7320 Å lines and affected by sky emission.

^c Blend of [O II] 7330 and 7331 Å lines and affected by sky emission.

Esteban et al. (1992) were the first who determined T_e for G2.4+1.4, but based on a rather low signal-to-noise spectrum of a zone close to our aperture no. 2. They obtain $T_e([\text{O III}]) \approx 12,000$ K, 1000-2000 K higher than our determinations. We derive $T_e([\text{N II}])$ for the first time in this object and in all apertures. The values of electron density are in the range 100-200 cm⁻³ except in the case

of aperture no. 2, for which $n_e([\text{S II}])$ and $n_e([\text{Cl III}])$ give consistent high values of about 1200 cm⁻³. This high-density zone corresponds to the brightest area of the nebula.

We obtain a fairly high value of T_e in S 308 – about 15,000 K –, and determine $T_e([\text{N II}])$ for the first time in this object. Esteban et al. (1992) obtained $T_e([\text{O III}])$ between 13,700 and 18,600 K

Table 5. Derredened line intensity ratios with respect to $I(\text{H}\beta) = 100$ for RCW 52, RCW 58 and S 308.

λ_0 (Å)	Ion	ID	$f(\lambda)$	RCW 52	$I(\lambda)/I(\text{H}\beta)$ RCW 58	S 308
3726.03	[O II]	1F	0.257	168.5 ± 5.6	24.2 ± 1.2	33 :
3728.82	[O II]	1F	0.256	209.0 ± 7.0	33.5 ± 1.4	52 ± 16
3734.37	H I	H13	0.255	–	2.19 ± 0.46	–
3750.15	H I	H12	0.253	–	4.14 ± 0.98	–
3770.63	H I	H11	0.249	–	3.88 ± 0.62	–
3797.9	H I	H10	0.244	–	3.59 ± 0.35	–
3819.61	He I	22	0.240	–	1.75 ± 0.44	–
3835.39	H I	H9	0.237	–	6.70 ± 0.55	–
3867.49	He I	20	0.230	–	–	134 ± 20
3868.75	[Ne III]	1F				
3888.65	He I	5	0.227	14.3 ± 4.8	31.3 ± 1.3	–
3889.05	H I	H8				
3964.73	He I	1F	0.211	–	3.20 ± 0.51	–
3970.07	H I	H7	0.210	–	15.77 ± 0.67	–
4026.21	He I	18	0.198	–	4.80 ± 0.74	–
4101.74	H I	H6	0.182	22.2 ± 3.3	30.75 ± 0.99	–
4340.47	H I	H γ	0.127	44.5 ± 3.3	48.9 ± 1.2	56 ± 13
4363.21	[O III]	2F	0.121	–	–	20.4 ± 5.8
4387.93	He I	51	0.115	–	1.00 ± 0.25	–
4471.09	He I	14	0.096	2.94 ± 0.99	8.84 ± 0.36	–
4630.54	N II	5	0.057	–	0.33 :	
4658.1	[Fe III]	3F	0.050	–	0.87 ± 0.22	11.1 ± 3.4
4713.14	He I	12	0.036	–	0.56 ± 0.18	–
4861.33	H I	H β	0.000	100.0 ± 2.3	100.0 ± 2.0	100.0 ± 6.6
4921.93	He I	48	-0.015	–	2.21 ± 0.34	–
4958.91	[O III]	1F	-0.024	11.80 ± 0.62	4.27 ± 0.27	280.5 ± 7.6
5006.84	[O III]	1F	-0.036	38.6 ± 1.9	14.14 ± 0.54	826 ± 19
5015.68	He I	4	-0.038	1.80 ± 0.60	4.46 ± 0.16	–
5517.71	[Cl III]	1F	-0.154	–	0.17 :	–
5537.88	[Cl III]	1F	-0.158	–	0.09 :	–
5754.64	[N II]	3F	-0.194	0.66 ± 0.13	1.11 ± 0.12	4.2 ± 1.3
5875.64	He I	11	-0.215	9.84 ± 0.50	25.45 ± 0.90	20.4 ± 2.0
6312.1	[S III]	3F	-0.283	0.65 ± 0.19		4.2 ± 1.3
6548.03	[N II]	1F	-0.318	40.0 ± 1.3	101.3 ± 3.6	43.8 ± 8.9
6562.82	H I	H α	-0.320	289.3 ± 8.7	310 ± 11	292 ± 12
6583.41	[N II]	1F	-0.323	118.8 ± 3.7	312 ± 11	131.6 ± 7.7
6678.15	He I	46	-0.336	2.96 ± 0.25	8.15 ± 0.37	5.80 ± 0.98
6716.47	[S II]	2F	-0.342	33.9 ± 1.2	10.58 ± 0.47	11.35 ± 0.97
6730.85	[S II]	2F	-0.344	29.5 ± 1.1	8.01 ± 0.36	8.0 ± 1.2
7065.28	He I	10	-0.387	1.78 ± 0.13	3.99 ± 0.34	3.21 ± 0.99
7135.78	[Ar III]	1F	-0.396	7.91 ± 0.35	4.66 ± 0.47	28.6 ± 3.8
7318.39 ^a	[O II]	2F	-0.418	2.12 ± 0.20	–	–
7319.99	[O II]	2F				
7329.66 ^a	[O II]	2F	-0.420	2.90 ± 0.24	–	–
7330.73	[O II]	2F				
9068.90	[S III]	1F	-0.585	22.0 ± 1.2	19.2 ± 1.4	48.5 ± 6.4
9530.60	[S III]	1F	-0.618	79.8 ± 4.8	59.9 ± 4.1	138 ± 22
Aperture size (arcsec ²)				8.0×1.0	8.0×1.0	8.0×1.0
$c(\text{H}\beta)$				1.35 ± 0.03	0.56 ± 0.04	0.17 ± 0.03
$F(\text{H}\beta)$ (10^{-14} erg cm ⁻² s ⁻¹)				1.43 ± 0.03	1.45 ± 0.03	0.24 ± 0.02

^a Blend of [O II] 7318 and 7320 Å lines and affected by sky emission.

^b Blend of [O II] 7330 and 7331 Å lines and affected by sky emission.

in different zones of S 308. All available determinations of n_e for this object are always below the low-density limit, $n_e < 100 \text{ cm}^{-3}$. Spectroscopical results of RCW 58 have been reported by Kwit-ter (1984); Rosa & Mathis (1990) and Stock et al. (2011) but none of these works could derive T_e from line intensity ratios. Therefore our value of $T_e(\text{N II})$ is the first direct determination of T_e

in RCW 58. Finally, this work presents the first determination of physical conditions and chemical abundances in RCW 52.

4.2 Ionic abundances from CELs

The use of large-aperture telescopes has permitted to obtain very deep spectra of the nebulae and to determine several ionic abun-

Table 6. Physical Conditions, ionic and total abundances for the apertures extracted in NGC 7635.

	A1 $t^2 = 0.0$	A2 $t^2 = 0.0$ $t^2 = 0.061$ ± 0.016		A3 $t^2 = 0.0$ $t^2 = 0.049$ ± 0.017		A4 $t^2 = 0.0$ $t^2 = 0.041$ ± 0.021		A5 $t^2 = 0.0$	A6 $t^2 = 0.0$
Physical conditions ^a									
n_e ([S II])	680 ± 110	150 ± 50		110 ± 60		2140 ± 290		220 ± 130	<100
n_e ([Cl III])	240 ⁺³⁷⁰ ₋₂₄₀	220 ⁺⁷⁵⁰ ₋₂₂₀		–		3290 ± 380		–	–
T_e ([N II])	8140 ± 160	8140 ± 510		8300 ± 400		9080 ± 100		8180 ± 470	7990 ± 450
T_e ([S II])	8260 ± 650	–		–		–		–	–
T_e (low)	8140 ± 160	8140 ± 510		8300 ± 400		9080 ± 100		8180 ± 470	7990 ± 450
T_e ([O III])	–	8010 ± 500		7670 ± 540		8690 ± 450		–	–
T_e ([Ar III])	8800 ± 910	–		–		8520 ± 830		–	–
T_e (high)	8800 ± 910	8010 ± 500		7670 ± 540		8650 ± 400		8180 ± 470	7990 ± 450
Ionic abundances ^b from collisionally excited lines									
N ⁺	7.48 ± 0.07	7.07 ± 0.07	7.37 ± 0.10	7.16 ± 0.05	7.38 ± 0.09	7.52 ± 0.02	7.67 ± 0.08	7.34 ± 0.07	7.37 ± 0.06
O ⁺	8.28 ± 0.19	7.95 ± 0.17	8.29 ± 0.14	8.05 ± 0.13	8.30 ± 0.13	8.17 ± 0.03	8.34 ± 0.09	8.20 ± 0.17	8.20 ± 0.17
O ²⁺	7.56 ± 0.14	8.29 ± 0.09	8.86 ± 0.11	8.30 ± 0.11	8.77 ± 0.11	7.60 ± 0.06	7.89 ± 0.12	7.95 ± 0.08	7.88 ± 0.08
Ne ²⁺	–	7.30 ± 0.24	7.94 ± 0.26	7.40 ± 0.36	7.93 ± 0.29	6.29 ± 0.17	6.61 ± 0.21	–	–
S ⁺	6.41 ± 0.07	5.73 ± 0.06	6.03 ± 0.10	5.84 ± 0.05	6.06 ± 0.09	6.28 ± 0.15	6.43 ± 0.14	6.04 ± 0.07	6.10 ± 0.06
S ²⁺	6.57 ± 0.34	7.04 ± 0.19	7.70 ± 0.26	7.11 ± 0.25	7.65 ± 0.28	6.94 ± 0.12	7.26 ± 0.21	6.65 ± 0.22	6.68 ± 0.28
Cl ²⁺	4.82 ± 0.14	5.17 ± 0.11	5.71 ± 0.20	5.21 ± 0.13	5.66 ± 0.21	4.99 ± 0.07	5.27 ± 0.17	5.06 ± 0.12	5.01 ± 0.16
Ar ²⁺	5.98 ± 0.12	6.32 ± 0.09	6.80 ± 0.17	6.29 ± 0.11	6.68 ± 0.18	6.01 ± 0.06	6.25 ± 0.15	6.17 ± 0.08	6.12 ± 0.09
Fe ²⁺	–	5.17 ± 0.18	5.76 ± 0.22	5.27 ± 0.41	5.75 ± 0.28	5.47 ± 0.07	5.77 ± 0.18	–	–
Ionic abundances ^b from recombination lines									
He ⁺	10.86 ± 0.01	10.84 ± 0.03		10.88 ± 0.03		10.78 ± 0.01		10.95 ± 0.02	10.88 ± 0.02
C ²⁺	–	8.30:		8.54:		8.15 ± 0.06		–	–
O ²⁺	–	8.86 ± 0.11		8.77 ± 0.10		7.99 ± 0.11		–	–
ADF(O ²⁺)	–	0.57 ± 0.14		0.47 ± 0.15		0.29 ± 0.13		–	–
Total abundances ^c									
He	11.04 ± 0.02	10.89 ± 0.04		10.97 ± 0.05		10.98 ± 0.03		11.10 ± 0.04	11.04 ± 0.04
C	–	8.44:		8.74:		8.57 ± 0.24		–	–
N	7.65 ± 0.08	7.54 ± 0.09	7.84 ± 0.11	7.53 ± 0.10	7.75 ± 0.13	7.68 ± 0.06	7.83 ± 0.10	7.60 ± 0.09	7.62 ± 0.07
O	8.36 ± 0.17	8.45 ± 0.08	8.96 ± 0.09	8.49 ± 0.09	8.90 ± 0.09	8.27 ± 0.03	8.47 ± 0.08	8.39 ± 0.12	8.37 ± 0.12
Ne	–	7.84 ± 0.28	8.48 ± 0.30	8.10 ± 0.43	8.63 ± 0.35	7.55 ± 0.51	6.96 ± 0.19	–	–
S	6.80 ± 0.38	7.08 ± 0.21	7.73 ± 0.29	7.15 ± 0.27	7.67 ± 0.31	7.03 ± 0.20	7.32 ± 0.26	6.75 ± 0.24	6.79 ± 0.31
Cl	5.02 ± 0.18	5.25 ± 0.11	5.79 ± 0.21	5.30 ± 0.13	5.88 ± 0.27	5.21 ± 0.18	5.49 ± 0.24	5.19 ± 0.13	5.15 ± 0.17
Ar	6.21 ± 0.12	6.40 ± 0.09	6.88 ± 0.18	6.41 ± 0.12	6.80 ± 0.19	6.25 ± 0.07	6.49 ± 0.16	6.35 ± 0.09	6.31 ± 0.10
Fe	–	5.52 ± 0.29	6.14 ± 0.30	5.61 ± 0.51	6.12 ± 0.35	5.95 ± 0.09	6.20 ± 0.24	–	–

^a n_e in cm⁻³; T_e in K.^b In units of 12+log(X^{n+}/H^+).^c In units of 12+log(X/H).

dances from CELs and, in some cases, also from RLs. Using CELs we have derived abundances of N⁺, O⁺, O²⁺, S⁺, S²⁺ and Ar²⁺ for all objects; Fe²⁺ for all nebulae except RCW 52; Ne²⁺ also for all except the low ionisation nebulae RCW 52 and RCW 58; Cl²⁺ for NGC 7635, NGC 6888 and G2.4+1.4 and Ar³⁺ only for G2.4+1.4. All the computations were made with PYNEB and using the atomic data listed in Table 5 of Esteban et al. (2014). We assumed a two zone scheme adopting T_e (low) for ions with low ionisation potential (N⁺, O⁺, S⁺, and Fe²⁺) and T_e (high) for the high ionisation potential ions (O²⁺, Ne²⁺, S²⁺, Cl²⁺, Ar²⁺ and Ar³⁺). Tables 6, 7, 8 and 9 show the ionic abundances and their uncertainties, which were computed taking into account the uncertainties in line fluxes,

T_e and n_e . We have considered two sets of abundances, one for $t^2 = 0$ and one for $t^2 > 0$, for those nebulae where the temperature fluctuations parameter, t^2 , can be estimated (see Section 4.5).

4.3 Ionic abundances from RLs

We detect several He I emission lines in the spectra of the ring nebulae. Although these lines arise mainly from recombination, those belonging to triplet transitions can be affected by collisional excitation and self-absorption effects. In order to minimize these effects, we determine the He⁺ abundance of the objects making use of PYNEB and the recent effective recombination coefficient compu-

Table 7. Physical Conditions, ionic and total abundances for the apertures extracted in NGC 6888.

	A1 $t^2 = 0.0$	A2 $t^2 = 0.0$	A3 $t^2 = 0.0$	A4 $t^2 = 0.0$ $t^2 = 0.83$ ± 0.019	A5 $t^2 = 0.0$ $t^2 = 0.071$ ± 0.014	A6 $t^2 = 0.0$ $t^2 = 0.069$ ± 0.016			
Physical conditions ^a									
n_e ([S II])	<100	310 ± 90	250 ± 150	150 ± 90	210 ± 140	200 ± 140			
n_e ([Cl III])	–	85 ⁺⁹⁸⁰ ₋₈₅	–	120 ⁺⁶⁴⁰ ₋₁₂₀	390 ⁺⁴⁸⁰ ₋₃₉₀	350 ⁺⁸³⁰ ₋₃₅₀			
T_e ([N II]) ^b	7700 ± 710	7480 ± 90	7630 ± 180	8950 ± 160	8840 ± 290	8860 ± 200			
T_e ([O III])	19040 ± 1130	12650 ± 400	9960 ± 640	10080 ± 970	9900 ± 540	9550 ± 820			
T_e ([Ar III])	–	8840:	9120 ± 1440	7500 ± 1070	7030 ± 540	7840 ± 1050			
T_e (high)	19040 ± 1130	12650 ± 400	9840 ± 590	9280 ± 740	8940 ± 400	9060 ± 650			
Ionic abundances ^c from collisionally excited lines									
N ⁺	7.48 ± 0.10	8.21 ± 0.03	8.25 ± 0.04	7.52 ± 0.02	7.88 ± 0.11	7.57 ± 0.04	7.87 ± 0.08	7.57 ± 0.03	7.86 ± 0.08
O ⁺	8.51 ± 0.28	8.29 ± 0.06	8.12 ± 0.08	7.45 ± 0.08	7.85 ± 0.13	7.45 ± 0.10	7.79 ± 0.10	7.52 ± 0.09	7.84 ± 0.11
O ²⁺	7.64 ± 0.05	7.53 ± 0.03	7.72 ± 0.07	8.06 ± 0.10	8.68 ± 0.11	8.12 ± 0.06	8.66 ± 0.09	8.09 ± 0.09	8.59 ± 0.08
Ne ²⁺	6.82 ± 0.14	6.62 ± 0.10	6.89 ± 0.16	7.36 ± 0.25	8.05 ± 0.27	7.42 ± 0.13	8.02 ± 0.18	7.38 ± 0.21	7.93 ± 0.20
S ⁺	6.26 ± 0.11	6.26 ± 0.03	6.14 ± 0.04	5.52 ± 0.03	5.87 ± 0.11	5.53 ± 0.05	5.83 ± 0.08	5.52 ± 0.04	5.80 ± 0.09
S ²⁺	–	6.10 ± 0.10	6.40 ± 0.19	6.76 ± 0.24	7.47 ± 0.28	6.90 ± 0.13	7.51 ± 0.19	6.84 ± 0.19	7.40 ± 0.20
Cl ²⁺	4.37 ± 0.16	4.44 ± 0.07	4.69 ± 0.09	4.82 ± 0.12	5.41 ± 0.21	4.93 ± 0.07	5.45 ± 0.15	4.90 ± 0.12	5.38 ± 0.16
Ar ²⁺	5.60 ± 0.05	5.81 ± 0.04	6.07 ± 0.08	6.30 ± 0.10	6.84 ± 0.18	6.36 ± 0.07	6.82 ± 0.13	6.35 ± 0.09	6.77 ± 0.14
Fe ²⁺	5.80 ± 0.20	5.39 ± 0.05	5.97 ± 0.05	6.04 ± 0.08	6.88 ± 0.23	6.07 ± 0.06	6.63 ± 0.16	5.97 ± 0.09	6.48 ± 0.17
Ionic abundances ^c from recombination lines									
He ⁺	10.91 ± 0.04	11.11 ± 0.01	11.19 ± 0.01	11.22 ± 0.01	11.22 ± 0.01	11.22 ± 0.01	11.22 ± 0.01	11.24 ± 0.01	11.24 ± 0.01
He ⁺⁺	–	–	8.14 ± 0.11	8.51 ± 0.09	8.42 ± 0.14	8.42 ± 0.14	8.42 ± 0.14	8.39 ± 0.10	8.39 ± 0.10
C ²⁺	–	8.29:	8.19:	8.52:	8.39:	8.39:	8.39:	8.34:	8.34:
O ²⁺	–	8.69:	8.40:	8.68 ± 0.11	8.66 ± 0.09	8.66 ± 0.09	8.66 ± 0.09	8.59 ± 0.07	8.59 ± 0.07
ADF(O ²⁺)	–	0.40:	0.68 ± 0.18	0.62 ± 0.15	0.54 ± 0.11	0.54 ± 0.11	0.54 ± 0.11	0.50 ± 0.12	0.50 ± 0.12
Total abundances ^d and abundance ratios									
He	–	11.13 ± 0.05	11.22 ± 0.13	11.23 ± 0.05	11.22 ± 0.01	11.22 ± 0.01	11.22 ± 0.01	11.23 ± 0.06	11.23 ± 0.06
O	8.56 ± 0.26	8.36 ± 0.07	8.27 ± 0.11	8.16 ± 0.13	8.74 ± 0.17	8.20 ± 0.05	8.71 ± 0.14	8.19 ± 0.13	8.66 ± 0.14
C	–	8.41:	8.38:	8.60:	8.61:	8.61:	8.61:	8.43:	8.43:
N	–	8.74 ± 0.18	8.58 ± 0.18	8.24 ± 0.18	8.60 ± 0.21	8.36 ± 0.15	8.66 ± 0.17	8.27 ± 0.18	8.56 ± 0.20
Ne	–	6.85 ± 0.13	7.43 ± 1.16	7.48 ± 0.70	8.17 ± 0.71	7.52 ± 0.24	8.12 ± 0.27	7.51 ± 0.78	8.06 ± 0.78
S	–	6.52 ± 0.11	6.60 ± 0.20	6.85 ± 0.26	7.55 ± 0.33	7.00 ± 0.15	7.60 ± 0.22	6.92 ± 0.21	7.47 ± 0.23
Cl	–	4.54 ± 0.19	4.79 ± 0.12	4.92 ± 0.15	5.51 ± 0.23	5.03 ± 0.09	5.55 ± 0.17	4.99 ± 0.15	5.47 ± 0.18
Ar	–	5.45 ± 0.06	6.13 ± 0.16	6.36 ± 0.12	6.90 ± 0.19	6.42 ± 0.08	6.88 ± 0.14	6.41 ± 0.11	6.83 ± 0.15
Fe	–	5.94 ± 0.11	6.39 ± 0.16	6.43 ± 0.19	7.33 ± 0.34	6.48 ± 0.18	7.09 ± 0.25	6.35 ± 0.20	7.06 ± 0.25

^a n_e in cm^{-3} ; T_e in K.

^b $T_e(\text{low}) = T_e(\text{[N II]})$ in all apertures.

^c In units of $12 + \log(X^{n+}/\text{H}^+)$.

^d In units of $12 + \log(X/\text{H})$.

tations by Porter et al. (2012, 2013) for He I lines, where both collisional contribution effects and the optical depth in the triplet lines are included. The final adopted He⁺ abundance is the weighted average of the ratios obtained from the individual brightest He I lines measured in each aperture and object and is included in tables 6, 7, 8 and 9. The number of He I lines used in each individual spectrum varies depending on its signal-to-noise ratio. Three lines were used in the case of S 308, five in RCW 52 and RCW 58, between two and five in the apertures of G2.4+1.4 and between 6 and 11 in the cases of NGC 6888 and NGC 7635. We detect He II 4686 Å line in all apertures of G2.4+1.4 due to the high ionisation degree of

the nebula, which is ionised by a very hot WO2 star. In the case of NGC 6888, we detect a rather faint He II 4686 Å line in apertures no. 3 to 6. We have determined the He²⁺ abundance using PYNEB and the effective recombination coefficient calculated by Storey & Hummer (1995). The He²⁺ abundances of NGC 6888 and G2.4+1.4 are shown in tables 7 and 8.

Pure RLs of multiplet 1 of O II have been detected and measured in most apertures of NGC 7635 and NGC 6888 (see figures 5 and 3, respectively), by the first time in the second object. We have determined the O²⁺ abundance from these lines making use of the effective recombination coefficients for case B and assuming LS

Table 8. Physical Conditions, ionic and total abundances for the apertures extracted in G2.4+1.4.

	A1	A2	A3	A4	A5
Physical conditions ^a					
n_e ([S II])	130 ± 50	1310 ± 220	220 ± 80	120 ± 70	120 ± 60
n_e ([O II])	–	1130 ± 270	–	–	–
n_e ([Cl III])	–	330:	–	1810:	–
T_e ([N II]) ^b	8520 ± 600	9060 ± 340	11260 ± 1620	9940 ± 1220	8600 ± 750
T_e ([S II])	–	15600 ± 4430	–	–	–
T_e ([O III])	–	10250 ± 910	–	10800 ± 1270	15400:
T_e ([S III])	–	8480 ± 420	–	–	–
T_e (high)	8520 ± 600	8900 ± 380	11260 ± 1620	10800 ± 1270	8600 ± 750
Ionic abundances ^c from collisionally excited lines					
N ⁺	7.83 ± 0.07	7.64 ± 0.04	7.31 ± 0.12	7.24 ± 0.12	7.72 ± 0.09
O ⁺	8.15 ± 0.33	8.16 ± 0.07	7.70:	7.54 ± 0.90	8.18 ± 0.47
O ²⁺	8.56 ± 0.10	8.47 ± 0.06	8.00 ± 0.18	8.22 ± 0.14	8.55 ± 0.12
Ne ²⁺	7.93:	8.04 ± 0.09	–	7.67 ± 0.45	8.06:
S ⁺	6.59 ± 0.07	6.88 ± 0.13	6.07 ± 0.12	6.03 ± 0.12	6.47 ± 0.09
S ²⁺	–	6.97 ± 0.04	–	6.48:	–
Cl ²⁺	5.84 ± 0.20	5.12 ± 0.17	–	5.00 ± 0.39	–
Ar ²⁺	6.48 ± 0.10	6.41 ± 0.07	5.96 ± 0.18	6.14 ± 0.14	6.42 ± 0.12
Ar ³⁺	–	5.73 ± 0.14	–	–	–
Fe ²⁺	–	6.40 ± 0.11	–	–	–
Ionic abundances ^c from recombination lines					
He ⁺	10.81 ± 0.03	10.91 ± 0.02	10.80 ± 0.08	10.89 ± 0.02	10.96 ± 0.05
He ²⁺	10.18 ± 0.07	10.45 ± 0.02	10.56 ± 0.07	10.39 ± 0.03	10.09 ± 0.09
C ²⁺	–	–	–	10.03 ± 0.16	–
Total abundances ^d and abundance ratios					
He	10.90 ± 0.03	11.04 ± 0.01	11.00 ± 0.06	11.01 ± 0.02	11.01 ± 0.04
O	8.79 ± 0.38	8.76 ± 0.09	8.27 ± 0.10	8.40 ± 1.70	8.79 ± 0.59
C	–	–	–	10.21 ± 0.17	–
N	8.44 ± 0.18	8.49 ± 0.06	7.87 ± 0.22	7.93 ± 0.29	8.09 ± 0.25
Ne	8.02:	8.17 ± 0.09	–	7.77 ± 0.54	8.14 ± 0.09
S	–	7.48 ± 0.14	–	6.80:	–
Cl	6.10 ± 0.10	5.43 ± 0.17	–	5.27 ± 0.45	–
Ar	6.66 ± 0.11	6.65 ± 0.07	6.12 ± 0.19	6.34 ± 0.16	6.55 ± 0.14
Fe	–	5.64 ± 0.23	–	–	–

^a n_e in cm⁻³; T_e in K.^b T_e (low) = T_e ([N II]) in all apertures.^c In units of 12+log(X^{n+}/H^+).^d In units of 12+log(X/H).

coupling calculated by Storey (1994) and considering T_e (high). As Ruiz et al. (2003) pointed out, the relative populations of the levels do not follow local thermodynamical equilibrium (LTE) for densities $n_e < 10^4$ cm⁻³. We use the prescriptions of Peimbert & Peimbert (2005) to calculate the appropriate corrections for the relative strengths between the individual O II lines.

The pure RL C II 4267 Å is detected in several apertures of NGC 7635 and NGC 6888, but only with relatively good signal-to-noise ratio – error lower than 40% – in aperture no. 4 of NGC 7635 (see Figure 6). We detected other C II lines in that aperture, but all of them are produced by fluorescence and not pure recombination. We also report an emission feature in aperture no. 4 of G2.4+1.4

at a wavelength that is consistent with C II 4267 Å but the identification is highly dubious (see Section 4.4 for a discussion about this issue). We compute the C²⁺ abundance from the measured flux of the C II 4267 Å RL, T_e (high), and the C II effective recombination coefficients calculated by Davey et al. (2000) for case B. The O²⁺ and/or C²⁺ abundances determined from RLs are included in tables 6, 7 and 8.

4.4 Total abundances

To compute the elemental or total abundances, we need to adopt a set of ionisation correction factors (ICFs) to correct for the un-

Table 9. Physical Conditions, ionic and total abundances for RCW 52, RCW 58 and S 308

	RCW 52	RCW 58	S 308
Physical conditions ^a			
n_e ([S II])	280 ± 150	100 ± 100	<100
n_e ([O II])	190 ± 90	<100	<100
T_e ([N II]) ^b	7200 ± 420	6450 ± 220	14930 ± 2900
T_e ([O III])	–	–	16800 ± 2500
T_e ([S III])	–	–	12420 ± 2200
T_e (high)	7200 ± 420	6450 ± 220	15020 ± 1720
Ionic abundances ^c from collisionally excited lines			
N ⁺	7.83 ± 0.07	8.41 ± 0.06	7.03 ± 0.16
O ⁺	8.87 ± 0.13	8.33 ± 0.09	6.85 ± 0.61
O ²⁺	7.52 ± 0.19	7.48 ± 0.08	7.95 ± 0.10
Ne ²⁺	–	–	7.55 ± 0.25
S ⁺	6.64 ± 0.09	6.26 ± 0.07	5.30 ± 0.17
S ²⁺	6.79 ± 0.15	6.93 ± 0.09	6.52 ± 0.10
Ar ²⁺	6.13 ± 0.20	6.18 ± 0.11	6.05 ± 0.16
Fe ²⁺	–	6.44 ± 0.21	6.28 ± 0.32
Ionic abundances ^c from recombination lines			
He ⁺	10.88 ± 0.03	11.24 ± 0.03	11.20 ± 0.04
Total abundances ^d and abundance ratios			
He	11.13 ± 0.05	11.46 ± 0.21	11.21 ± 0.08
O	8.91 ± 0.12	8.39 ± 0.08	7.98 ± 0.11
N	7.97 ± 0.08	8.60 ± 0.14	7.83 ± 0.60
Ne	–	–	7.62:
S	7.02 ± 0.18	7.02 ± 0.12	6.64 ± 0.25
Ar	6.42 ± 0.21	6.44 ± 0.24	6.15 ± 0.19
Fe	–	6.87 ± 0.38	6.82 ± 1.03

^a n_e in cm^{-3} ; T_e in K.

^b $T_e(\text{low}) = T_e(\text{[N II]})$ in all objects.

^c In units of $12 + \log(X^{n+}/\text{H}^+)$.

^d In units of $12 + \log(X/\text{H})$.

seen ionisation stages of each element. The O/H ratios are calculated simply adding O⁺ and O²⁺ abundances in all objects except G2.4+1.4. In this last object we see a very bright He II 4686 Å line, indicating a substantial amount of O³⁺. Although the He II line is also detected in some apertures of NGC 6888, its faintness indicates that the amount of O³⁺ is negligible ($\text{O}^{3+}/\text{O}^{2+} < 0.002$) and we will not take its contribution into account.

To derive He, C, N, Ne, S, Cl and Ar abundances - as well as O ones in the case of G2.4+1.4 - we have used the grid of models build by Delgado-Inglada et al. (2014) and stored in the 3MdB database (Morisset, Delgado-Inglada, & Flores-Fajardo 2015). From the models under the reference “PNe_2014”, for each observation of most of the nebulae, we select the models that simultaneously fit the following line ratios: [O III] 5007/[O II] 3727, He I 5876/H β and He II 4686/H β within 3, 3, and 5 times the observational error respectively. In the case of apertures no. 3, 4 and 6 of NGC 6888 and the single spectrum of RCW 58 we can only reproduce the [O III] 5007/[O II] 3727 and He II 4686/H β line ratios. We add to the selection criteria that the models must be radiation-

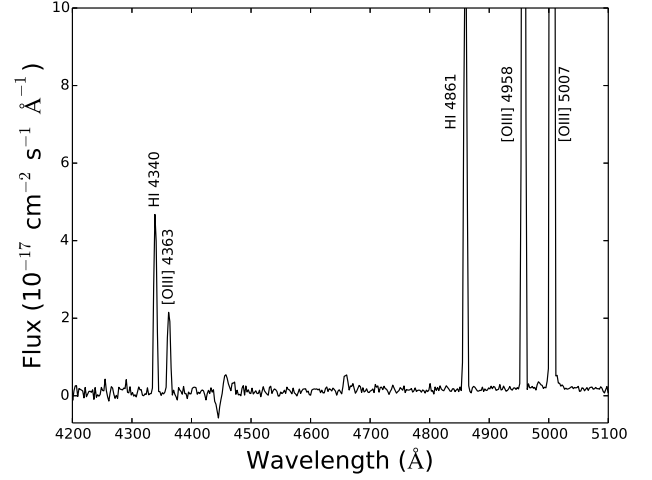


Figure 4. Section of the OSIRIS spectrum of aperture no. 1 of NGC 6888 –uncorrected for reddening– showing the abnormally intense auroral [O III] 4363 Å line in this external part of the nebula.

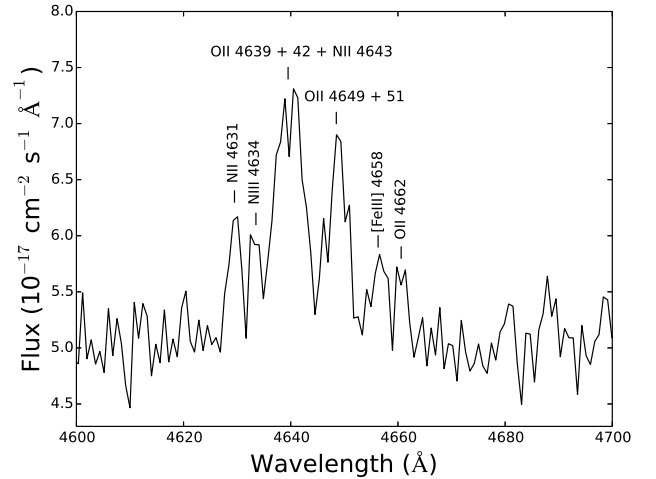


Figure 5. Section of the OSIRIS spectrum of aperture no. 3 of NGC 7635 –uncorrected for reddening– showing the recombination lines of multiplet 1 of O II about 4650 Å.

bounded or slightly matter bounded (i.e. the mass of the nebula being greater than 70% of the radiation-bounded case) and that the nebula is selected as “realistic” one (the field “com6” set to one, see Delgado-Inglada et al. 2014, for more details). The ionizing SED is described by Planck functions as well as T. Rauch models (Rauch 1997). These models have been run to determine ICFs for Planetary Nebulae (PNe), not for WR stars, but there are no most adapted models in 3MdB, especially that reach very high effective temperatures. For each observation, the selected models return the needed ICFs for each observed ion and the elemental abundances can be computed. Notice that the process allow us to obtain not a single value for the ICFs, but a set of values that correspond to all the models that reproduce the observational constraints, leading to an estimation of the uncertainties associated to each ICF. These

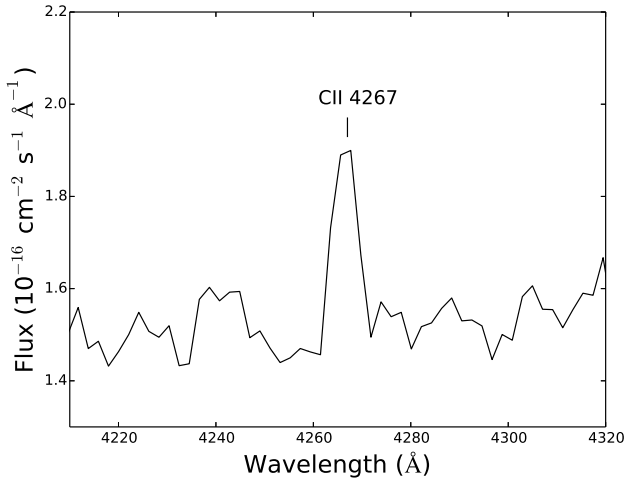


Figure 6. Section of the OSIRIS spectrum of aperture no. 4 of NGC 7635 –uncorrected for reddening– showing the recombination line of C II 4267 Å.

uncertainties are based on an implicit distribution of PNe models, that may not be totally adequate for the objects that we are studying here. We nevertheless think that the method at least give us an idea of the order of magnitude of the range in which we could find the “real” but inaccessible ICF. To illustrate the way we obtain the ICFs from the 3MdB data, in Figure 7 we plot the histograms of the ICF values of C⁺⁺, Ne⁺⁺, S⁺ + S⁺⁺, and Ar⁺⁺, for a single observation, namely aperture no. 4 of G2.4+1.4. The green dot indicates the median value and the red line runs over the standard deviation.

In the case of Fe, we have adopted the ICF scheme computed by Rodríguez & Rubin (2005) from observational data (their equation 3). Those authors also derived another ICF using photoionisation models but it seems to introduce an unexpected trend with the degree of ionisation (Delgado Inglada et al. 2009). As it can be noted in Table 7, we have not calculated total abundances for aperture no. 1 of NGC 6888. This is due no photoionisation models can reproduce the peculiar spectrum of this zone as well as the difference of about 11,000 K between $T_e([\text{O III}])$ and $T_e([\text{N II}])$. The characteristics of this particular spectrum will be discussed in Section 5.2.

4.5 Abundance discrepancy and temperature fluctuations

It is well known that ionic abundances determined from the intensity of CELs and RLs of the same ion do not coincide in nebulae. In the case of H II regions, the O²⁺ abundances derived from RLs are systematically a factor between 1.3 and 3 higher than those computed from CELs (e.g. García-Rojas & Esteban 2007). This dichotomy is called the abundance discrepancy problem and its origin is still unknown.

We computed the O²⁺/H⁺ ratios using CELs and RLs in three and five apertures of NGC 7635 and NGC 6888, respectively. As expected, the abundances obtained from RLs are larger than those determined from CELs in all spectra. We can quantify this difference defining the abundance discrepancy factor (hereafter ADF) as

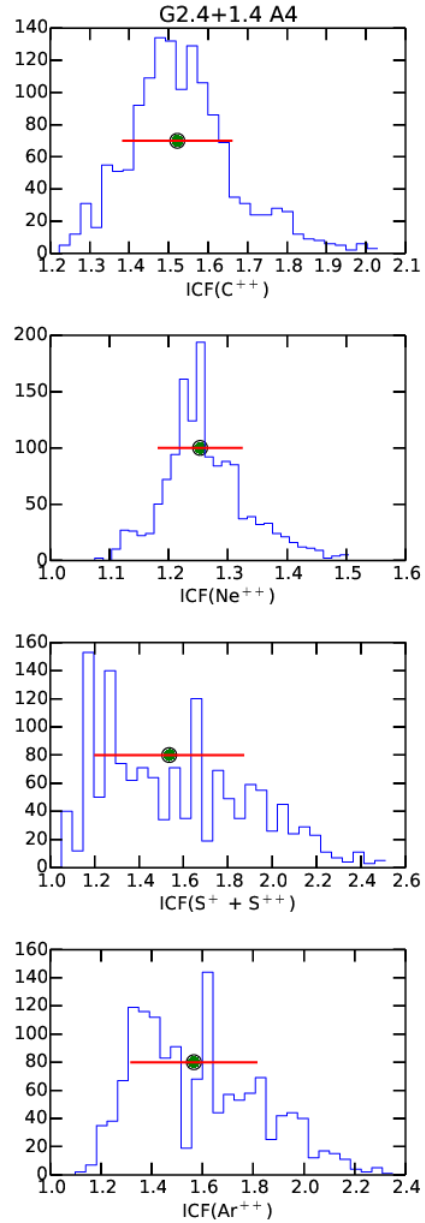


Figure 7. Histograms showing the frequency of the ICF values of C⁺⁺, Ne⁺⁺, S⁺+S⁺⁺, and Ar⁺⁺ provided by the photoionization models that reproduce the spectrum of aperture no. 4 of G2.4+1.4. The green dot indicates the median value and the red line runs over the standard deviation.

the difference between the logarithmic abundances derived from RLs and CELs:

$$\text{ADF}(X^{i+}) = \log(X^{i+}/H^+)_{\text{RLs}} - \log(X^{i+}/H^+)_{\text{CELs}}; \quad (1)$$

where Xⁱ⁺ corresponds to the ionisation state i of element X. The values of the ADF(O²⁺) found in NGC 7635 and NGC 6888 are shown in tables 6 and 7. The weighted mean of the individual ADF(O²⁺) of the different apertures of NGC 7635 and NGC 6888 are 0.38±0.12 and 0.50±0.06 dex, respectively. Both values are larger than the typical ADFs reported in the literature for Galactic and extragalactic H II regions (see e. g. García-Rojas & Esteban 2007), 0.26±0.09 dex, but more similar to the mean value found by

Esteban et al. (2014) for a sample of star-forming dwarf galaxies, which is 0.43 ± 0.16 dex.

There are several hypothesis to explain the origin of the abundance discrepancy problem. The earlier hypothesis is based on the presence of variations in the spatial distribution of T_e – the so-called temperature fluctuations, t^2 – in the ionised gas of nebulae (Torres-Peimbert et al. 1980). In the presence of such fluctuations, the abundances derived from RLs should be more representative of the true ones because abundances relative to hydrogen derived from RLs are almost independent on T_e , while those determined from CELs are strongly dependent on it. Classical photoionisation models do not predict significant temperature fluctuations but certain physical inhomogeneities in nebulae such as the presence of density variations may produce them (Viegas & Clegg 1994). Moreover, departures from a Maxwell-Boltzmann energy distribution of free electrons in nebulae in form of a “kappa-distribution” can mimic the effects of temperature fluctuations on the derived abundances (Nicholls et al. 2012) and could explain their ultimate nature.

Peimbert et al. (1991) explored the effects of shock waves in the spectra of ionised nebulae. They showed that large temperature fluctuations may arise in the presence of shocks with velocities larger than 100 km s^{-1} . From the observational point of view, there are some indications that the presence of shocks may be related with localized large values of t^2 and/or ADF in H II regions. Mesa-Delgado et al. (2009), from the analysis of the He I line ratios, found t^2 values in the shocked gas of the Herbig-Haro object HH 202-S of the Orion Nebula – $t^2 = 0.050$ – much larger than in the background nebular gas of the nebula – $t^2 = 0.016$. In addition, Mesa-Delgado et al. (2009) find a $\text{ADF}(\text{O}^{2+}) = 0.35$ for the shocked gas of HH 202-S, in contrast to the value of 0.11 found for the background gas. Moreover, the corresponding t^2 that these authors obtain assuming that the AD problem is produced by temperature fluctuations is in complete agreement with the t^2 value obtained from the He I line ratios. HH-204, also in the Orion Nebula, is another Herbig-Haro object showing indications that large t^2 values may be present in shocked nebular areas. Núñez-Díaz et al. (2012) find localized high values of T_e – about 1000 K larger than the surrounding gas – in the leading working surface of the shock related to HH-204. As we can see, one possible explanation of the larger ADFs and t^2 in ring nebulae may be the effects of shocks, more important than in H II regions due to their wind-blown nature. Going one step further, we can even speculate that the contribution of unresolved larger shocked areas in more distant starburst-dominated giant H II regions may also be the origin of their high temperature fluctuations and ADFs. In this context, ring nebulae as NGC 7635 and NGC 6888 would be interpreted as Galactic counterparts of those kinds of large-scale shock-contaminated nebulae.

If we assume the presence of spatial temperature fluctuations as the cause of the abundance discrepancy, then we have to correct abundances obtained from CELs. Under the temperature fluctuations paradigm, the structure of a gaseous nebula is characterized by two parameters: the average temperature, T_0 , and t^2 . For each nebula where we measure O II RLs – NGC 7635 and NGC 6888 – we can compute the T_0 that generates the same O^{2+}/H^+ ratio from CELs and from RLs. Then, with the corresponding value of t^2 , we can correct the abundances derived from CELs following the formalism firstly developed by Peimbert & Costero (1969). The computed ionic and total abundances for $t^2 > 0$ are presented in tables 6 and 7.

5 DISCUSSION

5.1 Abundance patterns

5.1.1 NGC 7635

Attending to spectroscopical and morphological considerations, the apertures observed in NGC 7635 can be separated into three groups in order to study the abundance pattern in this nebula. The first group is aperture no. 1 that corresponds to one of the brightest knots of S 162 – a large H II region that encompasses NGC 7635 and is ionised by the same O-type star. The second group corresponds to the brightest high-density “cometary” knot just at the southwest of the ionising star – aperture no. 4 – and the third one would include all the apertures that seem to be part of the main body of the bubble: apertures no. 2, 3, 5 and 6. In fact, all these apertures show lower n_e values and higher ionisation degree than the other two. The mean O/H and N/O ratios of the bubble apertures – considering determinations based on CELs and $t^2 = 0$ – are 8.43 ± 0.05 and -0.89 ± 0.08 dex, respectively. Talent & Dufour (1979) and Moore et al. (2002b) obtain values of about 8.49 and -1.3 dex for their “rim” zone, close to our apertures no. 2 and 3. The O/H and N/O ratios we obtain for S 162 are 8.36 ± 0.17 and -0.71 ± 0.19 dex, respectively, similar to the mean values obtained for the bubble apertures considering the errors. Moreover, the He/H ratios obtained for the bubble and S 162 are also consistent. As it can be seen in Table 12, the O/H, N/O and C/H ratios of NGC 7635 are the expected ones for an H II region located at the Galactocentric distance computed by Mesa-Delgado & Esteban (2010) assuming a Galactocentric distance of the Sun of $R_0 = 8.0 \pm 0.5$ kpc (Reid 1993). Therefore, we can conclude that the bubble of NGC 7635 should be composed by swept-up ambient gas.

The aperture no. 4 of NGC 7635 – corresponding to the bright dense knot – shows O/H and N/O ratios of 8.27 ± 0.03 and -0.57 ± 0.07 dex, respectively, which are slightly different from the bubble values. In their detailed study of *HST* data, Moore et al. (2002b) indicate that the knots close to the central star of NGC 7635 are the ionised edges of a large mass of neutral material, with strong photoevaporative flows toward the central star. Moore et al. (2002a) demonstrate that the strong density gradients of the knots may produce deviations in the spectrally derived elemental abundances at a level exceeding typical observational errors. Similar results have been found in localized high-density areas of the Orion Nebula. Mesa-Delgado et al. (2011, 2012) and Núñez-Díaz et al. (2012) have found that high-density bright bars, proplyds or Herbig-Haro objects inside the Orion Nebula show somewhat different O/H ratios with respect to the almost constant values obtained in the surrounding lower density zones. Those authors conclude that the different O/H ratios may be produced by the presence of dense gas with strong density stratification. In this particular situation, the values of physical conditions and ionic abundances derived using lines of low critical density may be unreliable, giving rise to wrong corrections for collisional de-excitation. This effect may be especially important in the calculation of $n_e([\text{S II}])$ from the [S II] 6716 and 6731 Å lines and the O^+/H^+ ratio derived from the [O II] 3726 and 3729 Å lines. All those lines have critical densities about $1-4 \times 10^3 \text{ cm}^{-3}$, of the order of the values we find for aperture no. 4. Assuming $n_e([\text{S II}])$ of about 7000 cm^{-3} we obtain a total O/H ratio of 8.43 for aperture no. 4, the ratio we obtain for the bubble. The use of this value of density produces a higher O^+ abundance but leaves O^{2+} virtually unaffected. In conclusion, we think that NGC 7635 should be chemically homogeneous and that strong lo-

Table 10. Ionization Correction Factors for NGC 7635 and NGC 6888.

Ratio	ICF ^a	NGC 7635					
		A1	A2	A3	A4	A5	A6
C/H	C ²⁺	–	1.39 ± 0.09	1.59 ± 0.18	2.64 ± 1.41	–	–
He/H	He ⁺ +He ²⁺	1.53 ± 0.08	1.13 ± 0.07	1.23 ± 0.12	1.58 ± 0.10	1.42 ± 0.13	1.44 ± 0.11
N/H	N ⁺	1.49 ± 0.16	2.95 ± 0.37	2.32 ± 0.46	1.43 ± 0.19	1.81 ± 0.22	1.76 ± 0.16
Ne/H	Ne ²⁺	–	3.4 ± 1.0	5.1 ± 1.9	18 ⁺²⁰ ₋₁₈	–	–
S/H	S ⁺ +S ²⁺	1.01 ± 0.01	1.04 ± 0.01	1.03 ± 0.01	1.00 ± 0.01	1.01 ± 0.01	1.01 ± 0.01
Cl/H	Cl ²⁺	1.59 ± 0.39	1.19 ± 0.03	1.23 ± 0.05	1.67 ± 0.62	1.36 ± 0.12	1.38 ± 0.08
Ar/H	Ar ²⁺	1.71 ± 0.11	1.20 ± 0.07	1.31 ± 0.13	1.73 ± 0.16	1.52 ± 0.14	1.55 ± 0.12
Fe/H	Fe ²⁺	–	2.2 ± 1.1	2.19 ± 0.94	2.99 ± 0.39	–	–

Ratio	ICF ^a	NGC 6888				
		A2	A3	A4	A5	A6
C/H	C ²⁺	1.31 ± 0.61	1.54 ± 0.60	1.22 ± 0.29	1.18 ± 0.16	1.22 ± 0.32
He/H	He ⁺ +He ²⁺	1.04 ± 0.12	1.08 ± 0.33	1.02 ± 0.12	1.01 ± 0.02	1.02 ± 0.14
N/H	N ⁺	3.4 ± 1.4	2.12 ± 0.88	5.2 ± 2.2	6.2 ± 2.1	5.0 ± 2.1
Ne/H	Ne ²⁺	1.69 ± 0.31	3.4 ^{+9.1} _{-2.4}	1.3 ^{+2.0} _{-0.3}	1.26 ± 0.57	1.3 ^{+2.3} _{-0.3}
S/H	S ⁺ +S ²⁺	1.07 ± 0.05	1.02 ± 0.03	1.16 ± 0.17	1.21 ± 0.16	1.15 ± 0.14
Cl/H	Cl ²⁺	1.26 ± 0.50	1.27 ± 0.23	1.25 ± 0.24	1.25 ± 0.18	1.24 ± 0.24
Ar/H	Ar ²⁺	1.14 ± 0.10	1.15 ± 0.36	1.15 ± 0.15	1.14 ± 0.12	1.14 ± 0.16
Fe/H	Fe ²⁺	3.56 ± 0.81	2.62 ± 0.89	2.47 ± 0.96	2.6 ± 1.0	2.4 ± 1.0

^a To be applied as: e.g. N/H = N⁺/H⁺ × ICF(N⁺).

Table 11. Ionization Correction Factors for G2.4+1.4, RCW 52, RCW 58 and S 308.

Ratio	ICF ^a	G2.4+1.4					RCW 52	RCW 58	S 308
		A1	A2	A3	A4	A5			
O/H	O ⁺ +O ²⁺	1.23 ± 0.03	1.32 ± 0.02	1.25 ± 0.06	1.26 ± 0.07	1.23 ± 0.34	–	–	–
C/H	C ²⁺	–	–	–	1.52 ± 0.14	–	–	–	–
He/H	He ⁺ +He ²⁺	–	–	–	–	–	1.78 ± 0.17	1.66 ± 0.80	1.03 ± 0.17
N/H	N ⁺	4.1 ± 1.6	7.05 ± 0.70	3.60 ± 1.54	4.9 ± 3.0	2.3 ± 1.3	0.14 ± 0.25	1.55 ± 0.47	6.3 ^{+8.5} _{-9.3}
Ne/H	Ne ²⁺	1.23 ± 0.03	1.34 ± 0.02	–	1.25 ± 0.07	1.20 ± 0.24	–	–	1.2 ^{+4.2} _{-1.2}
S/H	S ⁺ +S ²⁺	–	1.80 ± 0.06	–	1.54 ± 0.33	–	1.00 ± 0.01	1.01 ± 0.02	1.24 ± 0.40
Cl/H	Cl ²⁺	1.84 ± 0.09	2.05 ± 0.06	–	1.85 ± 0.27	–	–	–	–
Ar/H	Ar ²⁺	1.50 ± 0.11	1.74 ± 0.05	1.43 ± 0.17	1.57 ± 0.25	1.36 ± 0.19	1.96 ± 0.21	1.81 ± 0.88	1.27 ± 0.31
Fe/H	Fe ²⁺	–	2.92 ± 0.86	–	–	–	–	3.9 ± 1.3	3.4 ^{+7.7} _{-2.4}

^a To be applied as: e.g. N/H = N⁺/H⁺ × ICF(N⁺).

calized density stratification may be the reason of the somewhat lower abundances found in aperture no. 4.

Mesa-Delgado & Esteban (2010) found C/H ratios between 8.6 to 9.0 dex in several zones of NGC 7635, indicating an abnormally high abundance of this element. However, the comparison of the C/H ratios included in Table 12 indicates that the values we determine from our new observations are consistent with those expected from the abundance gradient. We have included the C/H ratio of aperture no. 4 in the table because: a) it is the best determination (the others have uncertainties larger than 40%) and b) the aforementioned problems associated with density stratification do not affect significantly the abundances determined from RLs. The emissivity of RLs show a much lower dependence on electron density and temperature than CELs.

5.1.2 NGC 6888

Kwitter (1981) and Esteban & Vilchez (1992) found N and He overabundances in NGC 6888 and established its stellar ejecta nature. On the other hand, the presence of chemical inhomogeneities in NGC 6888 has been a matter of debate. Esteban & Vilchez (1992)

found two main kinematical components with different chemical composition, a N-rich expanding bubble and an stationary ambient gas with normal abundances. Fernández-Martín et al. (2012) analysed integral field spectroscopy observations in several fields of NGC 6888, finding substantial spatial variations of the chemical composition of the ionised gas. They propose that the nebula is composed by three shells of different origin and chemical composition. Moreover, Stock & Barlow (2014) derived N/O ratios from FIR lines finding spatial variations of that ratio across the nebula. However, by means of photoionisation models, Reyes-Pérez et al. (2015) demonstrate those alleged abundance differences as effects of the ionisation structure within the nebula.

The comparison of the chemical abundances of NGC 6888 collected in Table 7 indicates that apertures no. 3 to 6 show fairly similar physical conditions and ionic abundances. These zones correspond to the bright filaments that conform the main body of the nebula (see Figure 1). As it has been commented in sections 4.1 and 4.4, aperture no. 1 shows very high values of $T_e([O III])$ and covers an external area of rather diffuse low density high-ionised gas (see Moore et al. 2000), with conditions and ionic abundances very different to the material of the filaments. Aperture no. 2 is

Table 12. Abundance comparisons in units of $12+\log(X/Y)$.

Nebula	d^a (kpc)	R_G^b (kpc)	(O/H) $^c_{\text{grad}}$	(O/H) $_{\text{obs}}$	(N/O) $^d_{\text{grad}}$	(N/O) $_{\text{obs}}$	(C/H) $^e_{\text{grad}}$	(C/H) $_{\text{obs}}$
NGC 7635 - bubble f	2.4 ± 0.2	9.2 ± 0.5	8.43 ± 0.07	8.43 ± 0.05	-0.99 ± 0.11	-0.89 ± 0.08	8.45 ± 0.14	8.57 ± 0.24^g
NGC 7635 - S162 h				8.36 ± 0.17		-0.71 ± 0.19		
NGC 6888 i	1.5 ± 0.5	7.8 ± 0.5	8.49 ± 0.07	8.20 ± 0.03	-0.93 ± 0.11	$+0.14 \pm 0.08$	8.59 ± 0.14	8.50:
G2.4+1.4 j	3 ± 1	5 ± 1	8.62 ± 0.07	8.77 ± 0.09	-0.82 ± 0.11	-0.27 ± 0.11	–	–
RCW 52	5.5	8.2	8.48 ± 0.07	8.91 ± 0.12	-0.95 ± 0.11	-0.94 ± 0.15	–	–
RCW 58	2.7	7.4	8.51 ± 0.07	8.39 ± 0.08	-0.92 ± 0.11	$+0.21 \pm 0.16$	–	–
S 308	1.5 ± 0.2	9.0 ± 0.5	8.44 ± 0.07	7.98 ± 0.11	-0.98 ± 0.11	-0.15 ± 0.82	–	–

^a References of the assumed distances are given in the text.

^b Galactocentric distances derived assuming the Sun at 8.0 kpc (Reid 1993).

^c Galactic radial gradient determined from O CELs (Esteban et al. 2015).

^d Galactic radial gradient determined from N and O CELs (Carigi et al. 2005).

^e Galactic radial gradient determined from C RLs (Esteban et al. 2005).

^f The observed values are the average of apertures no. 2, 3, 5 and 6 of NGC 7635.

^g The observed values of C/H are those of aperture no. 4 of NGC 7635.

^h The observed values are those of aperture no. 1 of NGC 7635.

ⁱ The observed values are the average of apertures no. 3, 4, 5 and 6 of NGC 6888.

^j The observed values are those of aperture no. 2 of G2.4+1.4.

also close to the edge of the nebula and, as aperture no. 1, it shows a T_e ([O III]) about 5000 K higher than T_e ([N II]), larger values of O/H and N/H ratios – but a N/O ratio similar to the filaments – and lower He abundance. We consider that the spectrum of aperture no. 2 may correspond to the mixing of emission from the filaments and the diffuse high-ionised gas that dominates aperture no. 1. In fact, as it can be seen in Figure 2 of Moore et al. (2000), the position of our aperture no. 2 corresponds to a tiny filament embedded in the [O III]-dominated tenuous gas. The mean values of the O/H, He/H and N/O ratios of apertures from no. 3 to no. 6 – the filaments – are 8.20 ± 0.03 , 11.22 ± 0.01 and $+0.14 \pm 0.08$ dex respectively (see also Table 12) confirming the important N and He enrichment – as well as an O deficiency – that NGC 6888 shows, in agreement with previous studies. The O/H, He/H, and N/O ratios obtained by Mesa-Delgado et al. (2014) for a zone almost coincident with our aperture no. 6, are in very good agreement with our results. Our determinations of the C/H ratio in this object have large uncertainties but seems to be fairly similar to the C/H ratio expected from the abundance gradient at the Galactocentric distance assumed by Mesa-Delgado et al. (2014, see Table 12). Therefore, there is not compelling reason to consider anomalous C/H ratios in this nebula as the previous results by Mesa-Delgado et al. (2014) suggested. This result would lead to the interesting result that the ON-cycle of the CNO burning has been more effective than the CN-cycle in the interior of the massive progenitor star of NGC 6888. This suspicion is also supported by the recent results obtained by Vamvatira-Nakou et al. (2016) from *Herschel* observations of M1-67, also a stellar ejecta nebula associated to a massive WR star. These authors determine the C/O from the photodissociation region (PDR) line fluxes finding it consistent with the solar C/O ratio within the errors.

5.1.3 G2.4+1.4

Due to the faintness of G2.4+1.4, its spectra are of comparatively much lower signal-to-noise ratio than those of NGC 7635 and NGC 6888 and abundance determinations are less precise for this object. The $12+\log(\text{O}/\text{H})$ shows a rather wide range of values from

8.27 to 8.79 in the different apertures. We must recall that the O abundance of this nebula is derived assuming an ICF(O), so it may be affected by biases difficult to estimate. On the other hand, the O abundances of apertures no. 1, 2 and 5 are very similar, but those of apertures no. 3 and 4 show lower values. It is interesting to note that these two last apertures show precisely the highest values of T_e and the lowest total abundances determined from CELs. The combination of both facts suggests that T_e may be somewhat overestimated in these zones or affected by localized shock heating in a manner similar to that detected in aperture no. 1 of NGC 6888 (see Section 5.2). A significant result is that although the O abundance shows some variation from one aperture to another, the N/O ratio is fairly constant. In Table 12 we compare the O/H and N/O ratios of aperture no. 2 – the spectrum with the best signal-to-noise ratio of this object – with the values expected from the Galactic abundance gradients. We have assumed the photometric distance of 3 ± 1 kpc determined by Dopita et al. (1990). The O/H ratio is somewhat high in G2.4+1.4, but seems to be consistent with the value of the O abundance expected at $R_G \sim 5$ kpc within the errors. The $\log(\text{N}/\text{O})$ of -0.27 is rather high and indicates some N-enrichment in the nebular gas. In the case of the He abundance, all the apertures except no. 1 give a mean $12+\log(\text{He}/\text{H})$ of about 11.02. Since there is not evidence of a radial abundance gradient of He in the Milky Way, all we can say is that the mean He/H ratio is consistent with that expected for the solar vicinity. Esteban et al. (1992) derived abundances in several zones of G2.4+1.4 and found an O abundance of 8.45 and a N/O ratio of -0.49 , values that agree with our determinations within the uncertainties. However, Esteban et al. (1992) also found a $12+\log(\text{He}/\text{H})$ of about 11.35, which is not confirmed with our deeper spectra. Summarizing, our results do not provide definitive evidence of chemical inhomogeneities in G2.4+1.4, only indications of a N enrichment.

As it has been commented in section 4.3, the C II 4267 Å line is only detected in aperture no. 4 of G2.4+1.4, and its intensity is abnormally high. The corresponding $12+\log(\text{C}/\text{H})$ results to be 10.21, an excessively high value even taking into account the relatively small Galactocentric distance of the nebula and the expected value of the C/H ratio extrapolating the radial C abundance gradient

determined by [Esteban et al. \(2005\)](#). We have inspected the spectra carefully finding no clear explanation for this oddity. Perhaps an artifact on the detector or an unknown emission feature is mimicking an emission line just at the wavelength of C II 4267 Å. We have to wait for an independent observational confirmation to ascertain whether this is a real feature or not.

5.1.4 RCW 52

This work presents the first abundance determinations of RCW 52. As it can be seen in [Table 12](#), the O/H ratio of 8.91 ± 0.12 is very high with respect to that expected for the Galactocentric distance of the nebula although its N/O is normal, so the object does not show traces of N enrichment. The He abundance of 11.13 ± 0.05 and also seems somewhat high. However, the ICF(He⁺) for this nebula is the largest one of the sample, so the exact value of He/H is highly uncertain. We have assumed the photometric distance of 5.5 kpc determined by [Reed \(1993\)](#) for this object.

5.1.5 RCW 58

There are two previous determinations of the chemical abundances of RCW 58 ([Kwitter 1984](#); [Rosa & Mathis 1990](#)), but both are based on an assumed value of T_e . Therefore, our set of abundances is the first one that has been determined using a direct determination of T_e , $T_e([\text{N II}])$ in this case. The comparison with the abundance gradients shown in [Table 12](#) confirms that the nebula is strongly N enriched. Moreover, the $12 + \log(\text{He}/\text{H})$ is 11.46 ± 0.21 , a very high value but affected by large uncertainties in the ICF(He). Although the O/H ratio is consistent with the abundance gradient within the errors, we cannot rule out some slight O deficiency in the object. We have assumed the photometric distance of 2.7 kpc determined by [Herald et al. \(2001\)](#) for this object.

5.1.6 S 308

The chemical abundances of S 308 were determined by [Kwitter \(1984\)](#); [Rosa & Mathis \(1990\)](#) and [Esteban et al. \(1992\)](#) and all of them found high N/O and He/H ratios in the nebula. Only [Rosa & Mathis \(1990\)](#) and [Esteban et al. \(1992\)](#) determined $T_e([\text{O III}])$ in this high-ionised object. In our case, we also determine consistent values of $T_e([\text{N II}])$ and $T_e([\text{S III}])$. The comparison with the abundance gradients shown in [Table 12](#) indicates that S 308 seems to be O-deficient in a higher degree than the N-rich filaments of NGC 6888. It also shows high N/H and He/H ratios. Considering that the O, N, Ne, S and Ar abundances – all elemental abundances determined from CELs – of S 308 are lower with respect to the rest of the objects, as well as its very high values of T_e , we cannot rule out the possibility that T_e may be overestimated due to an extra-heating of the gas due to shocks. We have assumed the distance of 1.5 kpc proposed by [Chu et al. \(2003\)](#) for S 308.

5.2 Shock excitation in aperture no. 1 of NGC 6888

As it has been commented in previous sections, aperture no. 1 of NGC 6888 shows a very high value of $T_e([\text{O III}])$ and we cannot derive its total abundances. This is because we can not find a photoionization model that reproduces its spectrum and, therefore, we lack of an appropriate set of ICFs. NGC 6888 shows X-ray emission that is especially bright in the northern part of the nebula (e.g.

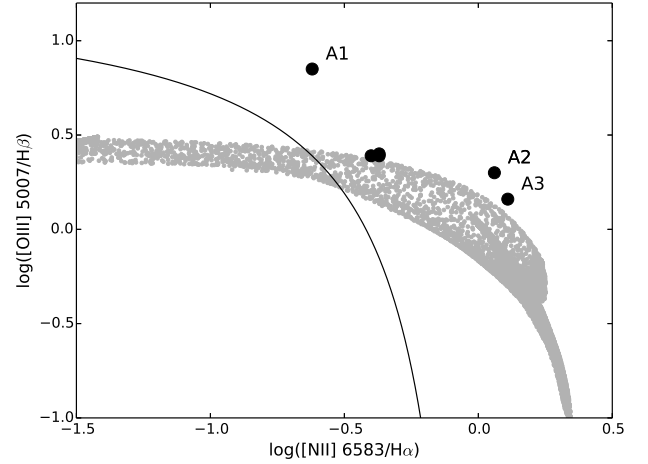


Figure 8. Diagnostic diagram of $[\text{O III}] 5007/\text{H}\beta$ vs. $[\text{N II}] 6583/\text{H}\alpha$. The solid line indicates the separation between photoionisation models of star-forming regions and AGNs as defined by [Kauffmann et al. \(2003\)](#) for their assumed metallicity. The grey points correspond to the photoionization model of NGC 6888 [Reyes-Pérez et al. \(2015\)](#). They do not fit the separation line because of the larger N/O ratio of the nebula. Black circles correspond to the spectra of the apertures of NGC 6888. The size of their errorbars are of the order or smaller than the circles. The three apertures at the north of the nebula, A1, A2 and A3 are indicated.

[Wrigge et al. 1994](#); [Toalá et al. 2014](#)), a feature that should be produced by collision between the WR wind and a preexisting circumstellar shell (e.g. [García-Segura et al. 1996](#)). The strong difference between $T_e([\text{O III}])$ and $T_e([\text{N II}])$ we find – in the sense that $T_e([\text{O III}])$ is higher than $T_e([\text{N II}])$ – is a common feature in the spectra of supernova remnants (e.g. [Fesen & Kirshner 1982](#); [Fesen et al. 1982](#); [Sankrit et al. 1998](#)). [Fernández-Martín et al. \(2012\)](#) indicate the possible presence of shocks in the northern area of NGC 6888. To illustrate that possibility in their Zone B, these authors compare their data with the library of fast radiative shock models of [Allen et al. \(2008\)](#). However, a drawback of the comparison made by [Fernández-Martín et al. \(2012\)](#) – especially important in the upper panel of their Figure 14 – is that the N/O ratio of NGC 6888 is almost one order of magnitude larger than solar, and the shock models they used assume a twice solar abundance. On the other hand, [Reyes-Pérez et al. \(2015\)](#) shows that photoionisation is the main excitation mechanism of NGC 6888 using their tailored photoionisation models and observational points in a BPT ([Baldwin, Phillips, & Terlevich 1981](#)) diagram (their Figure 7). In our Figure 8, we show an adaptation of Figure 7 of [Reyes-Pérez et al. \(2015\)](#) that represents $[\text{O III}] 5007/\text{H}\beta$ versus $[\text{N II}] 6584/\text{H}\alpha$ line intensity ratios. The solid line indicates the separation between photoionisation models of star-forming regions and active galactic nuclei (AGNs) as defined by equation 1 of [Kauffmann et al. \(2003\)](#). The grey points illustrate the individual spaxels of the 2D images obtained by [Reyes-Pérez et al. \(2015\)](#) from their photoionisation model of NGC 6888 that assumes chemical homogeneity in the nebula as well as abundances very similar to ours. As we can see, the points of the models spread in a relatively wide region of the diagram, indicating the rather different local ionisation conditions across the nebula. The black circles correspond to the line ratios measured in all apertures of NGC 6888. It is remarkable that the line defined by the observational points of apertures no. 2 to 6 is

roughly parallel to the general shape of the region of the photoionisation model. This indicates that the bulk of the gas of apertures no. 2 to 6 is photoionised. On the other hand, the point corresponding to the spectrum of aperture no. 1 is clearly above the photoionisation model and apart from the rest of the observational points. This indicates that its spectrum is not dominated by photoionisation, conversely, its position is consistent of having an important contribution of shock excitation (see also similar diagrams by Allen et al. 2008). Aperture no. 2 is also slightly above the photoionisation area suggesting some contamination of shock excitation.

5.3 Comparison with stellar evolution models

Esteban & Vilchez (1992) and Esteban et al. (1992) compared the abundance pattern of Galactic ejecta ring nebulae with the surface abundances predicted by the evolutionary models of massive stars of Maeder (1990). They found that the He, N and O abundances of the nebulae are consistent with the expected nucleosynthesis for stars with initial masses between 25 and 40 M_{\odot} at a given moment of the red supergiant (RSG) phase, prior to the WR stage. A similar initial stellar mass range was obtained by Garnett & Chu (1994) for the WN4 star Br 13 in the Large Magellanic Cloud, from abundances of its associated ejecta nebula. Mesa-Delgado et al. (2014) compared the He, C, N and O abundances they determine for NGC 6888 with the predictions of the stellar evolution models of Ekström et al. (2012) and Georgy et al. (2012). Their conclusions are also consistent with those obtained in previous works, the ionising star of NGC 6888 should have an initial mass between 25 and 40 M_{\odot} . A similar comparison has been made by Vamvatira-Nakou et al. (2016) in the case of M 1-67, finding a good fit for a central star of 32 M_{\odot} .

We have applied the same procedure followed by Mesa-Delgado et al. (2014) to our sample of ejecta ring nebulae in order to constrain the mass of their progenitor stars. We have used the set of mean He, C, N, O and Ne abundances determined for each object and the stellar evolution models of Ekström et al. (2012) and Georgy et al. (2012). We have considered rotational and non-rotational models for stars with initial masses of 25, 32, 40, 50 and 60 M_{\odot} . For the calculations, we have assumed that the stellar surface abundances given by the models are representative of the chemical composition of the stellar wind. The surface abundances of H, He, C, N, O, and Ne given by the models were weighted by the mass-loss rate and then integrated over time using the composite trapezoidal rule. In all the models, the initial integration point was set at the moment in which the massive star reaches the minimum effective temperature, T_{eff} , after finishing the main sequence (MS) stage. This point exactly coincides with the onset of enhanced mass loss at the beginning of the RSG phase (or luminous blue variable phase for the most massive stars) and, therefore, our approximation does not include material expelled during the MS stage. As Toalá & Arthur (2011) argued, the contribution of the material ejected during the MS can be ignored due to it is spread throughout a much more extended bubble with a size of several tens of parsecs, while the RSG and WR wind material would form a ring nebula in the immediate surroundings around the central star. To properly compare the model predictions with the observed abundances, the integration results for He, C, N, O, and Ne relative to H and/or O were converted from fractional mass to number units through the atomic weight of the elements. We used the He/H ratios to explore the variation of the He abundance because they are calculated from the intensity of RLs in both numerator and denominator. We also used the O abundance determined from RLs for determining the

C/O ratio in the case of NGC 6888. However, since the N and Ne abundances are always determined from CELs, we used their ratios with respect to the O abundances also derived from CELs for all the objects. Considering those particular abundance ratios, we avoid abundance discrepancy effects in the comparisons. In figures 9 to 12, we represent the assumed mean abundance ratios determined for NGC 6888, G2.4+1.4, S 308 and RCW 58 with respect to their He abundance and compare with the predicted abundance ratios of the stellar material ejected along time by the stellar models for 25, 32, 40, 50 and 60 M_{\odot} stars.

In Table 13 we compile some relevant data of the central star and the nebula of our stellar ejecta objects. We include the identifier of the star, its spectra type, rotational velocity and estimation of its present-day mass. In addition, we also include information about the binarity of the central star. In all the cases, we do not have clear indications of binarity and therefore we can consider them as single stars. Finally, we include the dynamical age estimated for the nebulae.

5.3.1 NGC 6888

Figure 9 shows the comparison for NGC 6888. This is the only object of our sample of WR ring nebulae for which we have derived the C abundance, and can compare the C/O ratios in addition to N/O and Ne/O ones. In Figure 9 we can see the important differences between the non-rotational models (upper panels) and rotational ones (lower panels). Though non-rotational models do not show significant differences for the nucleosynthesis produced by stars of initial masses between 25 and 40 M_{\odot} , the situation is completely different in the rotational case. One of the most important effects of the stellar rotation is that the WR phase starts much earlier than what is predicted by the non-rotational models. In figures 9 to 12 the onset of the WR phase is indicated by squares. In all cases, this was set following the definitions of stellar types of Eldridge et al. (2008) and the considerations discussed by Georgy et al. (2012). In the figures, we can see that rotational models of the 60 M_{\odot} star do not show a black square, this is because the models predict that the WR phase initiates during the MS stage in these stars.

An inspection of Figure 9 indicates that the C/O and N/O ratios of NGC 6888 are consistent with non-rotational models of 25 to 40 M_{\odot} and only with the rotational model of 25 M_{\odot} . In both cases, the fit between the observational data and models is produced for surface stellar abundances in a moment between the beginning of the SGR and before the onset of the WR phase. It must be noted that rotational models are calculated assuming a very large initial rotation velocity of about 300 km s^{-1} , much larger than the present-day value of 37 km s^{-1} calculated for the central star of NGC 6888 (see Table 13 and references therein). Therefore, the non-rotational models seem to be more appropriate for this particular object. In fact, the 25 to 40 M_{\odot} range we find with the non-rotational models agrees with the initial mass of about 32 M_{\odot} estimated by Georgy et al. (2013) from the stellar parameters of WR136 given by Hamann et al. (2006) and the HR diagram tracks calculated by Ekström et al. (2012). Another indication is the comparison between the dynamical age of the nebula with respect to the onset of the WR stage and the position of the observational points in the diagrams. NGC 6888 has a rather small dynamical age ($2-4 \times 10^4$ yr see Table 13) indicating that the enriched material of the nebula was ejected close to the onset of the WR phase. This situation is more consistent with the results obtained in the non-rotational case. Mesa-Delgado et al. (2014) determined the C/H ratio for NGC 6888 but they do not fit it with any stellar evolution

Table 13. Some relevant data of central stars and associated ejecta ring nebulae.

Nebula	Star	Spec. Type ^a	$v_{\text{rot}}^{\text{b}}$ (km s ⁻¹)	M_* (M_{\odot})	Binarity ^a	Dyn. Age ($\times 10^4$ yr)
NGC 6888	WR136	WN6	37	15 ^c	?	2–4 ^d
G2.4+1.4	WR102	WO2	–	$\sim 9^{\text{e}}$	–	8.8 ^f , 34 ^g
RCW 58	WR40	WN8	113	18–34 ^h	–	5.1 ^f
S 308	WR6	WN4	36	19 ^c	?	13.5 ^f

^a Data from the Galactic Wolf Rayet Catalogue v1.15 (<http://www.pacrowther.staff.shef.ac.uk/WRcat/>).

^b [Gräfener et al. \(2012\)](#).

^c Present-day stellar mass determined by [Hamann et al. \(2006\)](#).

^d [Freyer et al. \(2006\)](#).

^e Present-day stellar mass determined by [Tramper et al. \(2015\)](#).

^f [Gruendl et al. \(2000\)](#).

^g [Gosachinskij & Lozinskaya \(2002\)](#)

^h Present-day stellar mass determined by [Herald et al. \(2001\)](#).

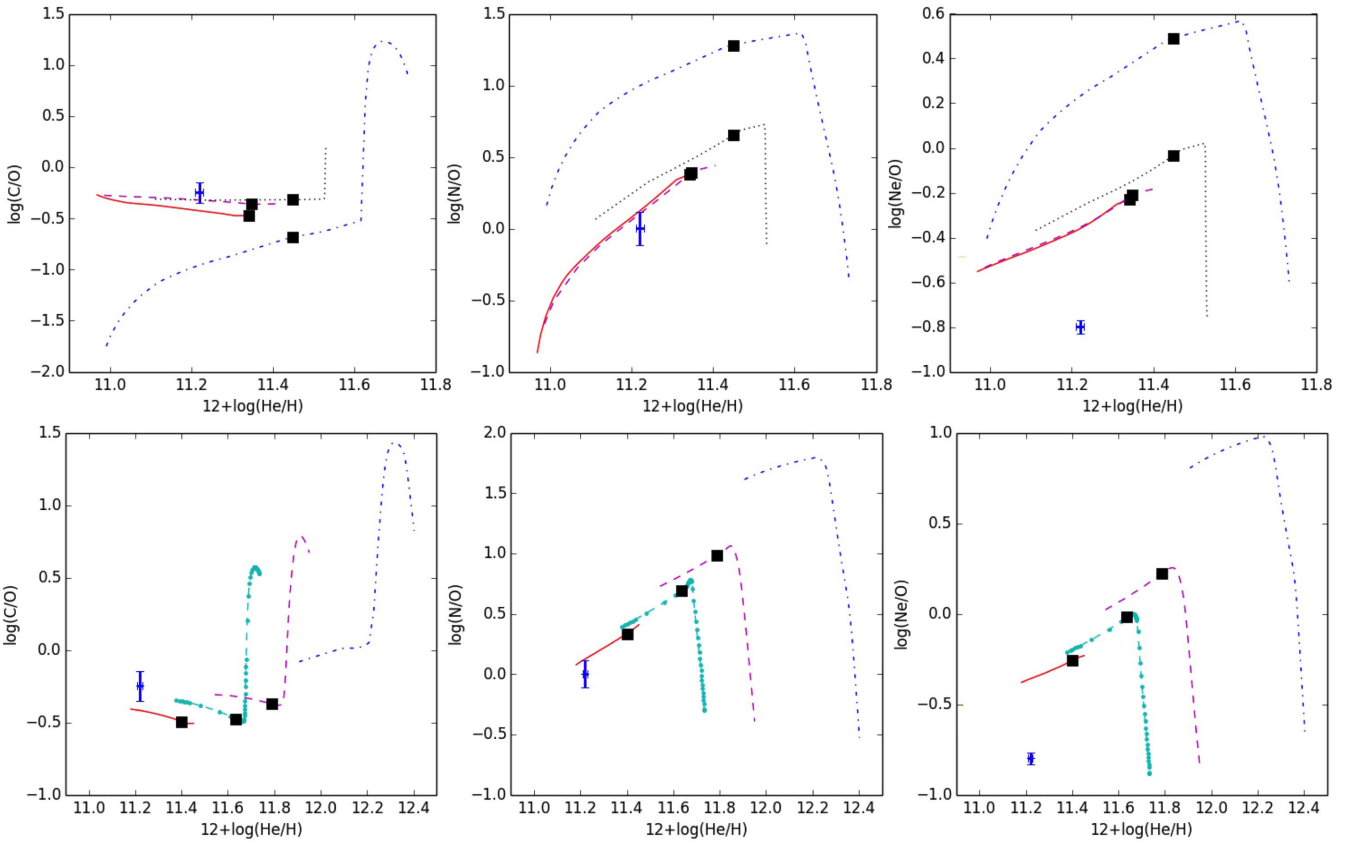


Figure 9. Abundance ratios of C/O, N/O and Ne/O as a function of the He abundance of the stellar material ejected by stars of different initial masses from non-rotation stellar evolution models (upper panels) and rotation ones (lower panels). The models are by [Ekström et al. \(2012\)](#). The blue point corresponds to our observed abundances for NGC 6888. The stellar masses represented are: $25 M_{\odot}$ (red solid line), $32 M_{\odot}$ (cyan dashed-big dotted line, only represented for rotational models), $40 M_{\odot}$ (magenta dashed line), $50 M_{\odot}$ (black dotted line, only represented for non-rotational models) and $60 M_{\odot}$ (blue dotted-dashed line). The black square indicates the onset of the WR phase for each model.

model (see their figures 4 and 5). Fortunately, our new determination of the C abundance from OSIRIS spectra does not show that disagreement. However, a problem with Ne/O ratio still persists. The Ne/O ratio we obtain – as well as the previous determination by [Mesa-Delgado et al. \(2014\)](#) – is between 0.3 and 0.5 dex lower

than the predictions of the stellar evolution models. This problem will be discussed in Section 5.3.5.

Note that we use the O/H ratio determined from CELs for calculating the observed N/O and Ne/O ratios and the O/H determined from RLs for C/O in Figure 9. The agreement between models and observations would be worse if we use O/H from CELs for C/O

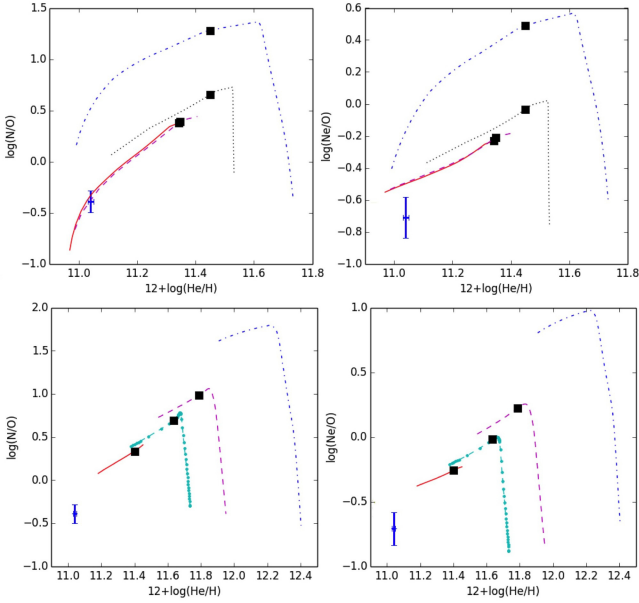


Figure 10. Same as Figure 9 for G2.4+1.4 and only including N/O and Ne/O ratios as a function of the He abundance.

and O/H from RLs for N/O and Ne/O. In this case the observation point would be displaced about +0.5 dex or –0.5 dex in ordinates, respectively. This is consistent with the idea that the AD problem is related to the kind of line that we are observing and that abundance ratios using the same kind of lines are less affected by the AD. On the other hand, the comparison between O/H ratios determined from CELs and RLs with the evolution of the O/H predicted by the models does not give an answer about which kind of lines gives the correct abundances. The comparison depends basically on the O/H ratio assumed by the models, which is $12+\log(\text{O}/\text{H}) = 8.66$. The observed O/H ratios observed from CELs are always below the 25, 32 and $40 M_{\odot}$ non-rotational models before the onset of the WR phase. Observed O/H ratios determined from RLs seem to be more consistent with the models.

5.3.2 G2.4+1.4

In the case of G2.4+1.4 and S 308, we can not derive C abundances and we only compare the N/O, Ne/O and He/H ratios with the predictions of stellar evolution models. Figure 10 shows the comparison between data and models for G2.4+1.4. We can see that the rotational models fail to reproduce the observations, but the non-rotational models of 25 to $40 M_{\odot}$ fit rather well the observed N/O vs. He/H ratios. [Tramper et al. \(2015\)](#) compare stellar parameters of Galactic WO stars and the HR diagram tracks provided by [Ekström et al. \(2012\)](#) and [Georgy et al. \(2012\)](#), finding that the likely progenitors of WO stars have initial masses of about 40-60 M_{\odot} . On the other hand, [Groh et al. \(2013\)](#) estimate that the progenitors of WO1-3 stars would be stars of initial masses higher than $40 M_{\odot}$, in the case of assuming the non-rotational models by [Ekström et al. \(2012\)](#) and [Georgy et al. \(2012\)](#) and equal or higher than $32 M_{\odot}$ assuming the rotational models. The rotational velocity of WR102 is actually unknown. Although [Sander et al. \(2012\)](#) report on a very high rotational velocity, [Tramper et al. \(2015\)](#) do not find any indication of rapid rotation in WR102. As we can see, only an initial mass of about $40 M_{\odot}$ for WR102 would reconcile the nebular and

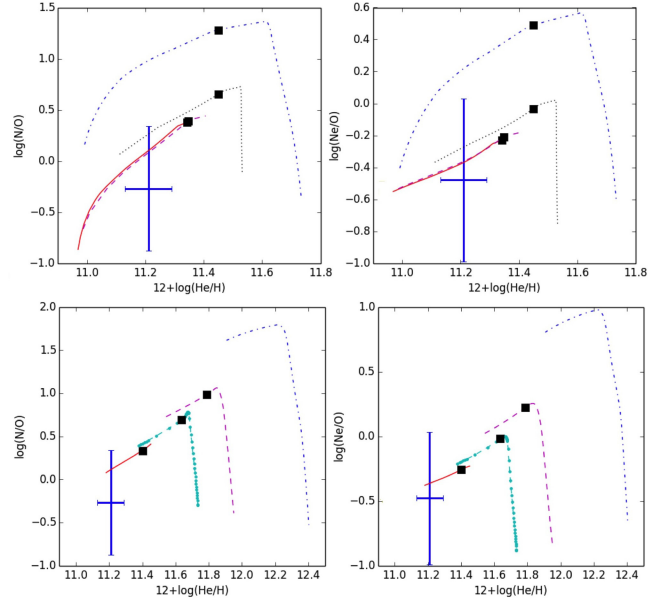


Figure 11. Same as Figure 10 for S 308.

stellar results. There are two estimations of the dynamical age of the nebula in the literature ([Gruendl et al. 2000](#); [Gosachinskij & Lozin-skaya 2002](#)) and they differ almost a factor four (see Table 13). The comparison of the N/O ratios shown in Figure 10 indicates that the stellar material should be ejected closer to the beginning of the RSG phase than to the onset of the WR stage. This would better agree with the higher value of the dynamical age of the nebula. [Tramper et al. \(2015\)](#) estimates that the central WO2 star of G2.4+1.4 (WR102) will explode as a SNic in less than 2000 yr. Therefore, G2.4+1.4 stands as an invaluable example of the pre-existent circumstellar medium in which the shock front of a SN explosion will develop.

5.3.3 S 308

Figure 11 compares the N/O, Ne/O and He/H ratios of S 308 with the predictions of stellar evolution models. The big error bars of the N/O and Ne/O ratios are due to the large uncertainties of the ICFs of N and Ne for this object. In fact, although its ICF(Ne) is very uncertain, we have assumed a nominal error of ± 0.30 dex for the Ne/O ratio. As we can see in Figure 11, both observed abundance ratios of S 308 (N/O and Ne/O vs. He/H) are consistent with the surface stellar abundances of non-rotational models of stars of initial masses between 25 and $50 M_{\odot}$. In the case of rotational models, the fit is only possible with stars of $25 M_{\odot}$. The present-day rotational value of WR6, the central star of S 308, is 36 km s^{-1} (see Table 13 and references therein) very far from the 300 km s^{-1} assumed in the rotational stellar evolution models. The dynamical age of the nebula is about $13.5 \times 10^4 \text{ yr}$ ([Gruendl et al. 2000](#)), so the ejection of the stellar material should be produced not far before the onset of the WR phase.

5.3.4 RCW 58

The low ionisation degree of RCW 58 does not permit to detect [Ne III] lines and to derive the Ne abundance. We can only com-

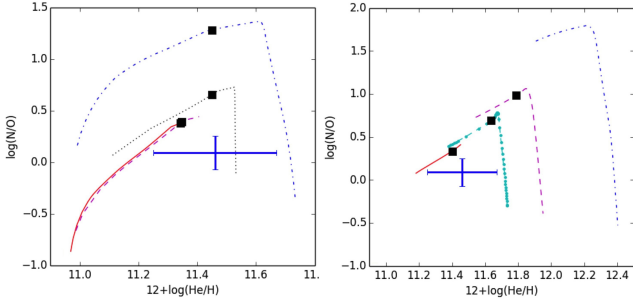


Figure 12. Same as Figure 9 for RCW 58 and only including N/O ratios as a function of the He abundance. Left panel: non-rotation stellar evolution models; right panel: rotation models.

pare the observed N/O and He/H ratios with the predictions of the stellar evolution models. In Figure 12 we present that comparison. The large uncertainty of the ICF(He) implies that the error bar of the He/H ratio is very large. The observational point does not fit the surface stellar abundances predicted by any model except for the non-rotational models of a $50 M_{\odot}$ star. However, the fit occurs at a point after the onset of the WR stage, which is not a reasonable solution because contradicts the current picture of the origin of stellar ejecta ring nebulae. If we assume that the He/H ratio of RCW 58 is overestimated by our ICF(He) and that our N/O is correct – this is directly based in the observations – the observational data may be consistent with the non-rotational models of 25 to $40 M_{\odot}$ and the rotational ones of $25 M_{\odot}$.

5.3.5 The low Ne/O ratios

Figures 9 and 10 indicate that the Ne/O ratios of NGC 6888 and G2.4+1.4 are below the model predictions for both, non-rotational and rotational models. This discrepancy was also reported in NGC 6888 by Mesa-Delgado et al. (2014). They find a $12+\log(\text{Ne}/\text{H})$ of 7.51 ± 0.20 , almost coincident with our mean value of 7.52 ± 0.01 , which are about 0.5 dex lower than the Ne abundance of the Orion Nebula, $12+\log(\text{Ne}/\text{H}) = 8.01 \pm 0.01$ (Rubin et al. 2011). Although Ne abundances are based on the assumption of an ICF(Ne), the large difference can not be explained solely by systematical uncertainties introduced by this parameter. To understand such underabundance of Ne, Mesa-Delgado et al. (2014) invoked the action of the NeNa cycle (e.g. Arnould & Mowlavi 1993). This cycle destroys Ne nuclei in the H-burning zone at temperatures of about 3.5×10^7 K, values that can be reached in massive star cores. Enhancement factors of 6-10 have been predicted by nucleosynthesis models (Woosley et al. 1995; Chieffi et al. 1998). Large Na abundances have been observed in the more massive yellow supergiants. Denissenkov (2005) has proposed that rotational mixing of Na between the convective core and the radiative envelope in the MS progenitors can account for the overabundances observed in those objects. Very recently, Huenemoerder et al. (2015) have reported a significantly enhanced Na abundance in the X-ray spectrum of the wind of WR6, the central star of S 308. They also interpret this overabundance as an effect of the NeNa cycle. The simultaneous strong action of ON – that we invoke to explain the O deficiency and almost normal C abundances seeing in NGC 6888 – and NeNa cycles may be due to very high temperatures in the H-burning zones of the progenitor stars of our WR nebulae. It is interesting to note that one of the possible scenarios to explain the Na-O

anticorrelation observed in globular clusters is based on the ejection of low-velocity material by previous generations of massive stars (e.g. Gratton, Carretta, & Bragaglia 2012). These stars should have experienced hot H-burning in order to alter the abundance of light elements with the simultaneous action of p-capture reactions of the CNO, NeNa, and MgAl chains (Denissenkov & Denisenkova 1989). Although the metallicities of the massive stars invoked to explain the pollution in globular clusters are extremely low in comparison with the solar one, it is very tempting to speculate about the possibility that objects similar to our WR ring nebulae may be the origin of the polluters of globular clusters.

6 CONCLUSIONS

We present very deep spectra of a sample of ring nebulae associated with evolved massive stars. Four of them associated to WR stars: NGC 6888, G2.4+1.4, RCW 58 and S 308 and two associated with O-type stars: NGC 7635 and RCW 52. The spectra have been obtained with OSIRIS and MagE spectrographs attached to the 10m GTC and the 6.5m Clay Telescope, respectively. We have obtained spectra for several slit positions or apertures in NGC 6888, NGC 7635 and G2.4+1.4 and for a single aperture in RCW 52, RCW 58 and S 308. We derive the physical conditions making use of several emission line intensity ratios as well as abundances for several ionic species from the intensity of CELs for all apertures. We obtain the first direct determination of T_e in the cases of RCW 52 and RCW 58. We derive the ionic abundances of C^{2+} and/or O^{2+} from faint RLs in several apertures of NGC 6888 and NGC 7635, permitting to derive their C/H and C/O ratios. This is the first time that O II lines are observed in NGC 6888. The comparison of the O^{2+}/H^+ ratios calculated from CELs and RLs permit to estimate the ADF in NGC 6888 and NGC 7635, finding rather high values. The ADFs are larger than the typical ones of normal H II regions in the Milky Way and other nearby spiral galaxies but similar to those found in the ionised gas of star-forming dwarf galaxies.

We do not find compelling evidence of chemical inhomogeneities in the nebulae where we have observed several apertures: NGC 6888, NGC 7635 and G2.4+1.4. We obtain $T_e([\text{O III}]) = 19040 \pm 1130$ K in a peripheral zone of NGC 6888, which is probably dominated by shock excitation. We find that since the two ring nebulae associated with O-type stars show normal chemical abundances, all the objects associated with WR stars show N enrichment. NGC 6888, RCW 58 and S 308 show also He enrichment and NGC 6888 and S 308 show some degree of O deficiency. The C abundance of NGC 6888 seems to be normal. This abundance pattern of the WR ring nebulae indicates the action of the nucleosynthesis of the CNO cycle and suggests an especially active ON cycle. NGC 6888 and G2.4+1.4 show lower Ne/O than expected, this may indicate the action of the NeNa cycle in a hot H-burning zone of the progenitor massive stars.

We have compared abundance ratios of our four WR ring nebulae with the surface chemical composition predicted by stellar evolution models of massive stars with initial masses from 25 to $60 M_{\odot}$ (Ekström et al. 2012; Georgy et al. 2012). We find that non-rotational models of stars of initial masses between 25 and $40 M_{\odot}$ seem to reproduce the abundance patterns in most of the objects, being this range wider in the case of S 308, from 25 to $50 M_{\odot}$. Only rotational models of $25 M_{\odot}$ show some fit with the data for NGC 6888, RCW 58 and S 308. As general result, the fit between models and observational data is produced in a moment between the beginning of the SGR and before the onset of the WR phase.

ACKNOWLEDGEMENTS

This paper is based on observations made with the Gran Telescopio Canarias (GTC), installed in the Spanish Observatorio del Roque de los Muchachos of the Instituto de Astrofísica de Canarias, in the island of La Palma and in data gathered with the 6.5 meter Magellan Telescopes located at Las Campanas Observatory, Chile. We are grateful to Josef Pössel and Stefan Binnewies (www.capella-observatory.com), Daniel López (IAC/INT), Rick Gilbert (Star Shadows Remote Observatory, SSRO) and Don Goldman (www.astrodonimaging.com) for give us permission to reproduce the astronomical images used in figures 1 and 2. This work has been funded by the Spanish Ministerio de Economía y Competitividad (MINECO) under project AYA2011-22614. JGR acknowledges support from Severo Ochoa excellence program (SEV-2011-0187) postdoctoral fellowship. AMD acknowledges support from the FONDECYT project 3140383 funded by the Chilean Government through CONICYT.

REFERENCES

- Allen M. G., Groves B. A., Dopita M. A., Sutherland R. S., Kewley L. J., 2008, *ApJS*, **178**, 20
- Arnould M., Mowlavi N., 1993, in Weiss W. W., Baglin A., eds, *Astronomical Society of the Pacific Conference Series Vol. 40, IAU Colloq. 137: Inside the Stars*. pp 310–323
- Baldwin J. A., Phillips M. M., Terlevich R., 1981, *PASP*, **93**, 5
- Cardelli J. A., Clayton G. C., Mathis J. S., 1989, *ApJ*, **345**, 245
- Carigi L., Peimbert M., Esteban C., García-Rojas J., 2005, *ApJ*, **623**, 213
- Cepa J., et al., 2000, in Iye M., Moorwood A. F., eds, *Society of Photo-Optical Instrumentation Engineers (SPIE) Conference Series Vol. 4008, Optical and IR Telescope Instrumentation and Detectors*. pp 623–631
- Cepa J., et al., 2003, in Iye M., Moorwood A. F. M., eds, *Society of Photo-Optical Instrumentation Engineers (SPIE) Conference Series Vol. 4841, Instrument Design and Performance for Optical/Infrared Ground-based Telescopes*. pp 1739–1749
- Chieffi A., Limongi M., Straniero O., 1998, *ApJ*, **502**, 737
- Chu Y.-H., Guerrero M. A., Gruendl R. A., García-Segura G., Wendker H. J., 2003, *ApJ*, **599**, 1189
- Davey A. R., Storey P. J., Kisielius R., 2000, **142**, 85
- Delgado Inglada G., Rodríguez M., Mampaso A., Viironen K., 2009, *ApJ*, **694**, 1335
- Delgado-Inglaterra G., Morisset C., Stasińska G., 2014, *MNRAS*, **440**, 536
- Denisenkov P. A., Denisenkova S. N., 1989, *ATsir*, 1538, 11
- Denissenkov P. A., 2005, *ApJ*, **622**, 1058
- Dopita M. A., Lozinskaya T. A., McGregor P. J., Rawlings S. J., 1990, *ApJ*, **351**, 563
- Dufour R. J., 1989, *Rev. Mexicana Astron. Astrofis.*, **18**, 87
- Ekström S., et al., 2012, *A&A*, **537**, A146
- Eldridge J. J., Izzard R. G., Tout C. A., 2008, *MNRAS*, **384**, 1109
- Esteban C., Vilchez J. M., 1992, *ApJ*, **390**, 536
- Esteban C., Vilchez J. M., Smith L. J., Clegg R. E. S., 1992, *A&A*, **259**, 629
- Esteban C., Smith L. J., Vilchez J. M., Clegg R. E. S., 1993, *A&A*, **272**, 299
- Esteban C., García-Rojas J., Peimbert M., Peimbert A., Ruiz M. T., Rodríguez M., Carigi L., 2005, *ApJ*, **618**, L95
- Esteban C., García-Rojas J., Mesa-Delgado A., Toribio San Cipriano L., 2014, *Astronomische Nachrichten*, **335**, 73
- Esteban C., García-Rojas J., Pérez-Mesa V., 2015, *MNRAS*, **452**, 1553
- Fernández-Martín A., Martín-Gordón D., Vilchez J. M., Pérez Montero E., Riera A., Sánchez S. F., 2012, *A&A*, **541**, A119
- Fesen R. A., Kirshner R. P., 1982, *ApJ*, **258**, 1
- Fesen R. A., Blair W. P., Kirshner R. P., 1982, *ApJ*, **262**, 171
- Freyer T., Hensler G., Yorke H. W., 2006, *ApJ*, **638**, 262
- García-Rojas J., Esteban C., 2007, *ApJ*, **670**, 457
- García-Segura G., Langer N., Mac Low M.-M., 1996, *A&A*, **316**, 133
- Garnett D. R., Chu Y.-H., 1994, *PASP*, **106**, 626
- Georgy C., Ekström S., Meynet G., Massey P., Levesque E. M., Hirschi R., Eggenberger P., Maeder A., 2012, *A&A*, **542**, A29
- Georgy C., Walder R., Folini D., Bykov A., Marcowith A., Favre J. M., 2013, *A&A*, **559**, A69
- Gosachinskij I. V., Lozinskaya T. A., 2002, *Astronomy Letters*, **28**, 701
- Gräfener G., Vink J. S., Harries T. J., Langer N., 2012, *A&A*, **547**, A83
- Gratton R. G., Carretta E., Bragaglia A., 2012, *A&ARv*, **20**, 50
- Groh J. H., Meynet G., Georgy C., Ekström S., 2013, *A&A*, **558**, A131
- Gruendl R. A., Chu Y.-H., Dunne B. C., Points S. D., 2000, *AJ*, **120**, 2670
- Hamann W.-R., Gräfener G., Liermann A., 2006, *A&A*, **457**, 1015
- Hamuy M., Suntzeff N. B., Heathcote S. R., Walker A. R., Gigoux P., Phillips M. M., 1994, *PASP*, **106**, 566
- Herald J. E., Hillier D. J., Schulte-Ladbeck R. E., 2001, *ApJ*, **548**, 932
- Howard I. D., Murray J., 1990, *SERC Starlink User Note No. 50*
- Huenemoerder D. P., et al., 2015, *ApJ*, **815**, 29
- Kauffmann G., et al., 2003, *MNRAS*, **346**, 1055
- Kwitter K. B., 1981, *ApJ*, **245**, 154
- Kwitter K. B., 1984, *ApJ*, **287**, 840
- Luridiana V., Morisset C., Shaw R. A., 2015, *A&A*, **573**, A42
- Maeder A., 1990, *A&AS*, **84**, 139
- Marshall J. L., et al., 2008, *SPIE*, **7014**, 701454
- Martins F., Schaerer D., Hillier D. J., 2005, *A&A*, **382**, 999
- Massey P., Strobel K., Barnes J. V., Anderson E., 1988, *ApJ*, **328**, 315
- Mesa-Delgado A., Esteban C., 2010, *MNRAS*, **405**, 2651
- Mesa-Delgado A., Esteban C., García-Rojas J., Luridiana V., Bautista M., Rodríguez M., López-Martín L., Peimbert M., 2009, *MNRAS*, **395**, 855
- Mesa-Delgado A., Núñez-Díaz M., Esteban C., López-Martín L., García-Rojas J., 2011, *MNRAS*, **417**, 420
- Mesa-Delgado A., Núñez-Díaz M., Esteban C., García-Rojas J., Flores-Fajardo N., López-Martín L., Tsamis Y. G., Henney W. J., 2012, *MNRAS*, **426**, 614
- Mesa-Delgado A., Esteban C., García-Rojas J., Reyes-Pérez J., Morisset C., Bresolin F., 2014, *ApJ*, **785**, 100
- Mitra P., 1991, PhD thesis, Rice University, Houston, TX.
- Moore B. D., Hester J. J., Scowen P. A., 2000, *AJ*, **119**, 2991
- Moore B. D., Hester J. J., Scowen P. A., Walter D. K., 2002a, *AJ*, **124**, 3305
- Moore B. D., Walter D. K., Hester J. J., Scowen P. A., Dufour R. J., Buckalew B. A., 2002b, *AJ*, **124**, 3313
- Morisset C., Delgado-Inglaterra G., Flores-Fajardo N., 2015, *RMxAA*, **51**, 103
- Nazé Y., Chu Y.-H., Points S. D., Danforth C. W., Rosado M., Chen C.-H. R., 2001, *AJ*, **122**, 921
- Nicholls D. C., Dopita M. A., Sutherland R. S., 2012, *ApJ*, **752**, 148
- Núñez-Díaz M., Mesa-Delgado A., Esteban C., López-Martín L., García-Rojas J., Luridiana V., 2012, *MNRAS*, **421**, 3399
- Oke J. B., 1974, *ApJS*, **27**, 21
- Oke J. B., 1990, *AJ*, **99**, 1621
- Peimbert M., Costero R., 1969, *Boletín de los Observatorios Tonantzintla y Tacubaya*, **5**, 3
- Peimbert A., Peimbert M., 2005, *RMxAC*, **23**, 9
- Peimbert M., Sarmiento A., Fierro J., 1991, *PASP*, **103**, 815
- Porter R. L., Ferland G. J., Storey P. J., Detisch M. J., 2012, *MNRAS*, **425**, L28
- Porter R. L., Ferland G. J., Storey P. J., Detisch M. J., 2013, *MNRAS*, **433**, L89
- Raymond J. C., Hester J. J., Cox D., Blair W. P., Fesen R. A., Gull T. R., 1988, *ApJ*, **324**, 869
- Rauch T., 1997, *A&A*, **320**, 237
- Reed B. C., 1993, *PASP*, **105**, 1465
- Reid M. J., 1993, *ARA&A*, **31**, 345
- Reyes-Pérez J., Morisset C., Peña M., Mesa-Delgado A., 2015, *MNRAS*, **452**, 1764
- Rodríguez M., 1999, *A&A*, **348**, 222
- Rodríguez M., Rubin R. H., 2005, *ApJ*, **626**, 900
- Rosa M. R., Mathis J. S., 1990, in Garmay C. D., ed., *Astronomical Society of the Pacific Conference Series Vol. 7, Properties of Hot Luminous Stars*. pp 135–138

- Rubin R. H., Simpson J. P., O'Dell C. R., McNabb I. A., Colgan S. W. J., Zhuge S. Y., Ferland G. J., Hidalgo S. A., 2011, *MNRAS*, **410**, 1320
- Ruiz M. T., Peimbert A., Peimbert M., Esteban C., 2003, *ApJ*, **595**, 247
- Sander A., Hamann W.-R., Todt H., 2012, *A&A*, **540**, A144
- Sankrit R., et al., 1998, *ApJ*, **504**, 344
- Simón-Díaz S., Herrero A., Sabín-Sanjulián C., Najarro F., Garcia M., Puls J., Castro N., Evans C. J., 2014, *A&A*, **570**, L6
- Smith L. J., Nota A., Pasquali A., Leitherer C., Clampin M., Crowther P. A., 1998, *ApJ*, **503**, 278
- Smith L. J., Stroud M. P., Esteban C., Vilchez J. M., 1997, *MNRAS*, **290**, 265
- Stock D. J., Barlow M. J., 2014, *MNRAS*, **441**, 3065
- Stock D. J., Barlow M. J., Wesson R., 2011, *MNRAS*, **418**, 2532
- Storey P. J., 1994, *A&A*, **282**, 999
- Storey P. J., Hummer D. G., 1995, *MNRAS*, **272**, 41
- Talent D. L., Dufour R. J., 1979, *ApJ*, **233**, 888
- Toalá J. A., Arthur S. J., 2011, *ApJ*, **737**, 100
- Toalá J. A., Guerrero M. A., Gruendl R. A., Chu Y.-H., 2014, *AJ*, **147**, 30
- Torres-Peimbert S., Peimbert M., Daltabuit E., 1980, *ApJ*, **238**, 133
- Tramper F., et al., 2015, *A&A*, **581**, A110
- Vamvatira-Nakou C., Hutsemékers D., Royer P., Waelkens C., Groenewegen M. A. T., Barlow M. J., 2016, *A&A*, **588**, A92
- Viegas S. M., Clegg R. E. S., 1994, *MNRAS*, **271**, 993
- Woolley S. E., Langer N., Weaver T. A., 1995, *ApJ*, **448**, 315
- Wrigge M., Wendker H. J., Wisotzki L., 1994, *A&A*, **286**, 219

This paper has been typeset from a $\text{\TeX}/\text{\LaTeX}$ file prepared by the author.